

AD-A103 178

FLOW RESEARCH CO KENT WA

F/6 8/12

MODELING THE MECHANICAL ENERGY BUDGET OF THE BEAUFORT SEA ICE C--ETC(U)

DEC 79 R S PRITCHARD, M D COON, D R THOMAS

N00014-79-C-0147

UNCLASSIFIED

FLOW-RR-137R

NL

1 of 1
 Δ|| Δ
 C.S. 1.7.11

END
DATE
FILMED
9-81
DTIC

LEVEL II

13.5
2

FLOW RESEARCH COMPANY

A DIVISION OF FLOW INDUSTRIES, INC.

AD A103178



DTIC
ELECTE
S **D**
AUG 24 1981
D

HEADQUARTERS
21414 - 68th Avenue South
Kent, Washington 98031 (206) 872-8500
Seattle Ex. 622-1500 TWX 910-447-2762

DISTRIBUTION STATEMENT A

Approved for public release;
Distribution Unlimited

81 7 17 082

5
ENC FILE COPY

| | |
|----------------------------|-------------------------------------|
| Accession For | |
| NTIS GRA&I | <input checked="" type="checkbox"/> |
| DTIC TAB | <input type="checkbox"/> |
| Unannounced | <input type="checkbox"/> |
| Justification | |
| By <u>Pex Lts. on file</u> | |
| Distribution/ | |
| Availability Codes | |
| Dist | Avail and/or Special |
| A | |

LEVEL II

2

12

Flow Research Report No. 137R

**6 Modeling the Mechanical Energy Budget
of the Beaufort Sea Ice Cover.**

Contract N00014-79-C-0147

by

S. Pritchard

D. Coon

D. R. Thomas

December 1979

FLOW-RR-137R

**Flow Research Company
A Division of Flow Industries, Inc.
Kent, Washington 98031
(206) 854-1370**

**DTIC
SELECTE
AUG 24 1981**

D

**DISTRIBUTION STATEMENT A
Approved for public release;
Distribution Unlimited**

90439

Modeling the Mechanical Energy Budget of the

Beaufort Sea Ice Cover

by

Robert S. Pritchard

Max D. Coon

D. R. Thomas

Flow Research Company

21414 - 68th Avenue South

Kent, Washington 98031

Abstract

The mechanical energy balance for the sea ice cover of the Beaufort Sea portion of the Arctic Ocean has been used to evaluate a parameter study on the strength of a plastic sea ice model. The results of this study show that a hardening plastic model with a diamond shaped yield surface and a compressive strength of 1.0 to $1.5 \times 10^5 \text{ Nm}^{-1}$ will simulate the winter behavior of ice in the Beaufort Sea accurately.

The mechanical energy (power) budget utilizing a hardening plastic model was examined for a seventeen day period during the winter of 1976. The study period included two storms (extreme ice motion events) during which the power from the atmosphere is transferred to the sea ice cover and redistributed horizontally by the divergence of the stress flux, concentrating the dissipation of mechanical energy in the sea ice cover along the north slope of Alaska. These results show how the power from the atmosphere over the entire Beaufort Sea can be concentrated to ridge and raft sea ice and generate acoustic energy in the ocean along the margins of the Beaufort Sea.

Introduction

In temperate regions the transfer of mechanical energy between the atmosphere and the ocean has been studied (e.g., Holland, 1978). At high latitudes where the ocean is ice covered during some seasons of the year, the transfer of mechanical energy is altered and only recently (Coon and Pritchard, 1979) has the concept of mechanical energy balance been introduced in such a way as to include sea ice. This concept provides a simple description of the transfer of energy through the atmosphere/ice/ocean system and explains how the ice cover dissipates energy by deformation and transfers energy horizontally by stress flux divergence.

The dissipation of mechanical energy in the sea ice cover results in ridging, rafting and the generation of acoustic energy. Coastal processes, such as beach erosion and sediment transport, are also altered by the presence of the ice cover and its effect on the mechanical energy budget. Therefore, understanding how the mechanical energy from the atmosphere is transferred to the sea ice cover and subsequently redistributed and dissipated within the ice cover leads to an understanding of these physical phenomena.

In this paper a seventeen day period during the winter of 1976 is examined for the Beaufort Sea. The energy budget is used to evaluate a parameter study of strength and yield surface shapes for a plastic ice sea model. Material parameters in the model are optimized and the tuned model is subsequently used to study the energy budget of the atmosphere/ice/ocean system. This study shows how the energy from the atmosphere distributed over the ice cover of the Beaufort Sea can be concentrated and dissipated along the north slope of Alaska and the

Canadian Archipelago. During these periods of high energy dissipation, severe ridging, rafting occur in these marginal seas.

Test Conditions

From January 27 through February 12, 1976, winds in the Beaufort Sea (see Figure 1 for the region considered) cause ice behavior that is both interesting and useful for testing ice model response. During this time period two storms pass through the Beaufort Sea causing large motions, first to the west and later to the east. The second storm lasts beyond the test period. During that time the entire ice cover remains motionless, even though strong winds persist. A brief description of the day-to-day activity follows.

On January 27 and 28, while moderate easterly winds blow in a band about 200 km wide off the Alaska north slope, the ice remains stationary. On January 29, a high pressure region begins to move eastward across the northern edge of the Beaufort Sea (above the grid boundary Figure 1). Westward ice motions begin at the western edge of the region. By January 31, the entire region is moving westward (from Barrow to Banks Island) except for a wide belt of fast ice along the Alaska north slope. The fast ice region is shoreward of the flaw lead running from Barrow to Banks Island and about 150 km offshore near Prudhoe Bay. During this time a series of north-south running leads opens uniaxially with the lead system appearing first at the western edge of the region and then moving eastward with the storm. Finally a 50 km wide lead appears along Banks Island. The winds die down on February 1, and come about. There is little activity through February 5.

On February 6, a low pressure area to the north of the region of interest causes westerly winds to rise over most of the region. The ice

begins to move eastward. Then winds strengthen to give an air stress of about 0.4 Pa and the ice moves toward Banks Island with substantial shearing along the Alaska north slope. The previous fast ice region then moves with the pack. By February 8, the ice nearest Banks Island stops moving because the open water and thin ice have been eliminated by ridging. Ice strength increases so that the stress can resist the wind force. This region spreads so that by February 10, the entire Beaufort Sea is motionless even though strong winds continued to blow after the end of the test period on February 12.

During this time period there are twenty data buoys and three manned camps located in the region of interest. These provide accurate motions and winds to test the response of the model (Pritchard, et al., 1977). Therefore, in addition to the energy variables, there are velocity, deformation and data available to support the results.

Sea Ice Model

The mathematical model under consideration in this work is a modified version of the AIDJEX plastic ice model (Coon, et al., 1974; Pritchard, 1975; Rothrock, 1975; Thorndike, 1975). In the momentum balance equation this model accounts for air stress τ_a , water stress τ_w , Coriolis force $-mfk \times v$, sea surface tilt $mg \nabla H$ and internal stress divergence $\nabla \cdot \sigma$.

$$m \dot{v} = \tau_a + \tau_w - mf k \times v - mg \nabla H \quad (1)$$

where v is ice velocity and m is area mass density. The ice stress is related to deformation by an elastic-plastic constitutive law. Yield strength depends on the instantaneous thickness distribution at each location so that hardening or softening can occur with deformation. The thickness distribution describes the relative fraction of ice of each

thickness category and the concentration of each category changes as the ice deforms through ridge and lead formation. Details of model formulation and parameters are available in the AIDJEX final report to the National Science Foundation (Coon, et al., 1978). A brief description of material parameters is given by Coon and Pritchard (1979). In the present work the strength parameter variations are performed for a simpler model in which yield strength (magnitude and shape of yield surface) is assumed fixed for a given calculation. The yield surface is then varied for different calculations to determine the effect of this parameter. Previous work by Pritchard et al., (1977) has shown that the ideal plastic model (no hardening/softening) provides daily average velocity and strain results that are nearly equal to those obtained for the hardening/softening model if a sequence of daily winds is used in place of the constantly varying winds. The shape of the yield surface will be varied in this parameter study between a teardrop, triangle and diamond shape as shown in Figure 2. Boundary layer drag coefficients are unchanged for all runs.

Mechanical Energy Balance

Consider a large scale element of ice, say tens of kilometers across, composed of many individual ice floes, leads and ridges (Figure 3). At the top surface of the element of ice, the wind works on the ice at the rate $p_a = \vec{v} \cdot \vec{\tau}_a^T$ which is the product of the air stress acting on the ice and the ice velocity. Each term in p_a may be considered an average over the area which is reduced to a point by a standard limiting argument. At the bottom surface of the ice element, the ice works on the ocean at the rate of $p_o = -\vec{v} \cdot \vec{\tau}_w^T$ where τ_w is the traction exerted on the ice by the ocean.

Around the sides of the ice element, the stress field produces a traction $\underline{\underline{\sigma}} \underline{\underline{n}}$ where $\underline{\underline{\sigma}}$ is actually a stress resultant (the Cauchy stress in excess of hydrostatic equilibrium integrated through the ice thickness), $\underline{\underline{n}}$ is the unit outward normal to the side of the ice element. The rate at which work per unit area is done on the ice element by this traction is

$$p_f = \frac{1}{A} \oint_L \underline{\underline{v}}^T \underline{\underline{\sigma}} \underline{\underline{n}} d\ell \quad (2)$$

where L is the curve defining the horizontal area A of ice element. From the Green-Gauss theorem this power input at the sides may be expressed as the divergences of the stress flux $p_f = \nabla \cdot (\underline{\underline{v}}^T \underline{\underline{\sigma}})$, which is the horizontal transfer of energy by the nonhomogeneous velocity and stress fields. In this development, the velocity field is assumed continuous.

The remaining force acting on the ice element that contributes to the mechanical energy budget is gravitational and is important only when the sea surface is tilted. The rate of increase of gravitational potential energy as the ice moves up the sloped surface H is

$$p_g = \underline{\underline{v}}^T m g \nabla H$$

where m is the mass of the ice element and g is the gravitational constant.

The mechanical energy balance is obtained by equating the resultant of work done by all forces acting on the ice element to the sum of the rate of work done by internal stress accompanied by deformation

$p_d = \text{tr } \underline{\underline{\sigma}} \underline{\underline{D}}$ where $\underline{\underline{D}}$ is the stretching, and rate of change of kinetic energy $\kappa = \frac{1}{2} m \underline{\underline{v}}^T \underline{\underline{v}}$. Therefore,

$$\dot{K} + p_d = p_a - p_o - p_g + p_f \quad (3)$$

This result is identical to that of Coon and Pritchard (1979) who introduced $p_w = p_o + p_g$ as the total power transferred into the ocean. Although the present decomposition into power input to the ocean by the water drag force τ_w and the rate of increase of gravitational potential energy is useful for understanding the physical importance of each term, we use the total power to the ocean p_w in the remainder of the analysis primarily because p_g is small and there is no difference in interpretation of results.

In the present work, a seventeen day period is studied as a sequence of daily response. For time resolution on the order of one day, a quasi-steady analysis is adequate. Thus, rate of change of kinetic energy is ignored and the sequence of instantaneous values satisfies

$$p_a + p_f = p_w + p_d \quad (4)$$

The power input to the ice from the atmosphere p_a is calculated from the air stress $\tau_a = \rho_a c_a ||U_g|| B_a U_g$ where U_g is the geostrophic wind, B_a is a rotation operator through angle α (ccw) and $\rho_a c_a$ is air density times a drag coefficient. It is satisfactory to think of the air stress τ_a as the input variable (Pritchard, et al., 1977).

The water stress is $\tau_w = \rho_w c_w ||v - v_g|| B(v - v_g)$ where $\rho_w c_w = 5.5 \text{ kg/m}^3$ is water density times a drag coefficient and v_g is the geostrophic ocean current that is assumed to be constant in time for all calculations (e.g., Pritchard, et al., 1977).

The global form of mechanical energy balance is

$$P_a + P_f = P_w + P_d \quad (5)$$

where for each term

$$P = \frac{1}{A} \int_R p \, da$$

and each term in Equation (4) is the area average of its counterpart in Equation (3).

One additional relationship that is required is the free drift power input p_{afd} . This term is the power that would be input locally to the ice from the atmosphere if the ice cover were present but ice stress were zero. For this case $\underline{\sigma} = \underline{0}$ implies $p_f = p_d = 0$ so that all free drift energy is input locally to the ocean. Thus,

$$p_{afd} = p_{wfd} \quad (6)$$

and a similar global form follows directly.

Results

Data from ten calculations with the plastic sea ice model are presented a) to show how the energy transfer is altered by changing strength of the ice, b) to show how the information may be used to verify and tune material parameters, and c) to identify important contributions to the mechanical energy budget during winter when ice is compact and stress is important.

Strength Variations

A set of eight simulations during the first eight days of the test period (January 27 - February 3, 1976) is performed using a perfectly plastic model. Each calculation uses a different yield surface size and/or shape. A teardrop, triangle or diamond shape (Figure 2) is chosen and strength varies from 10^4 Nm^{-1} to 10^6 Nm^{-1} . In addition a

free drift calculation is performed to describe the limiting case of zero ice strength.

The actual power input to the ice from the atmosphere is presented in Figure 4. This curve represents the average power P_a over the region of interest. To calculate this variable, a set of triangles connecting data buoy and manned camp locations is constructed as shown in Figure 1. The local power $p_a = v_o^T T_a$, where v_o is observed station velocity, is then integrated over each triangle assuming linear variations of p_a within the triangle. Finally, contributions from all triangles are weighted by area and summed to determine the area average.

The power input to the ice is observed to be small until the latter half of January 29, rising to 25 mW/m^2 late on January 30. The power input then drops to a negligible value by the end of January 31 and remains low through February 3. As the storm arrives (1200 GMT on January 29 through 2100 GMT on January 30), the increase in energy input is caused largely by the increased area of ice that moves. Winds and ice speeds of the moving region are less variable. But as the storm passes, the drop in power input is caused by falling winds and ice speeds over the whole region.

The free drift power available P_{afd} is also shown on Figure 4. While similar in shape, it is seen that P_{afd} is approximately twice as large as the observed value. The difference is attributed to the effect of ice stress since other model results have shown the boundary layer models to be accurate at this time (Pritchard, et al., 1977; Pritchard, 1977). The free drift power available is nearly proportional to wind speed cubed at higher winds. The increasing wind intensity is shown clearly in this display. In fact, it is felt that free drift power

available is a useful variable to determine which times are of interest for modeling ice behavior. In this display, storms are amplified to show their strength in a significant measure - the power available in the region.

The three calculations titled, Runs 3B, C and D, were reported by Pritchard, et al. (1977). The air stress used in Run 3 is in error on January 30 (Pritchard, et al., 1977). The values input the model are too large by about 30 percent, therefore, when model results are compared with observed values, they should be scaled down accordingly. The power P_a and P_w should be reduced to about 60 percent of calculated values for Run 3 results on January 30 because both air stress and velocity must be reduced, whereas observed power input should be lowered to about 70 percent because only τ_a affects it. The velocity fields in Run 3B are judged to be nearly the same as free-drift. It is seen that the sequence of daily values shown in Figure 4 for Run 3B agrees to within 2 mW/m^2 with free drift power available. This confirms the conclusion that for yield strengths of 10^4 Nm^{-1} the velocity field is essentially free drift. On the other hand, the velocity fields calculated in Run 3C, using a yield strength of 10^5 Nm^{-1} , represent observed velocities reasonably well. The energy input for Run 3C (and the continuous run using the same model) exceeds observed values by about 50 percent of the peak observed value on January 30 and 31. When scaled down to correct for the air stress error, the power input is nearly correct.

As pointed out by Pritchard (1977), the teardrop shaped yield surface incorrectly simulates the uniaxial opening of a large-scale lead system because large tractions exist across the open leads. It was

shown that either a triangle or diamond yield surface could correct this deficiency. When a triangle yield surface with a strength $p^* = 10^5 \text{ Nm}^{-1}$ (Run 3E) is used to simulate ice behavior on January 30, the deformation and stress fields showed uniaxial opening of North-South running leads with no traction across them. Furthermore, a flaw lead is generated about 200 km offshore, only slightly seaward of the correct location, and the velocity field is satisfactory. The power input from this one-day simulation is shown on Figure 4. The power input of 12 mW/m^2 is about 30 percent lower than the observed value for that day. This value is closer than previous calculations, but, when considered along with the flaw lead position, indicates that yield strength is too high.

The calculation labeled Run 3J gives results nearly identical to Run 3E. This occurs because the entire region is either opening or shearing with no substantial convergence. For these stretching states a diamond with strength $p^* = 2 \times 10^5 \text{ Nm}^{-1}$ and a triangle with $p^* = 1 \times 10^5 \text{ Nm}^{-1}$ admit the same stress states (See Figure 2). The triangle is the largest concave yield surface that is contained by the tensile cutoff lines and a given yield strength p^* . Since an extreme shape is unlikely in practice, the study uses the intermediate diamond shape.

Three more calculations of January 30 with the diamond yield surface and strengths of 1×10^5 (Run 3H), 1.5×10^5 (Run 3I) and $10 \times 10^5 \text{ Nm}^{-1}$ (Run 3K) show how the power input varies with this parameter (Figure 4). It is seen that $p^* = 1.5 \times 10^5 \text{ Nm}^{-1}$ (Run 3I) reproduces the observed power input. The results of Runs 3H and K provide a wider range variation. From the power input a diamond yield surface with $p^* = 1.5 \times 10^5 \text{ Nm}^{-1}$ is best. The velocity and deformation fields for

Runs 3H, I, J and K show that the flaw lead moves seaward with increasing strengths and that both fields are accurate when strength is about $1-1.5 \times 10^5 \text{ Nm}^{-1}$. When the air stress error is considered, the lower strength, $p^* = 1 \times 10^5 \text{ Nm}^{-1}$ is felt to be best. The velocity field at the larger strength (Run 3J) is actually more accurate than Run 3H because the eastern part of the region is more accurate. When strength is increased to $10 \times 10^5 \text{ Nm}^{-1}$ (Run 3K) results are similar to Run 3D in which the flaw lead is far offshore and the motion is dominated by buoy motions at the boundaries.

Figure 5 shows the power input to the ocean P_w . Here again, the diamond yield surface fits the observed values well on January 30. The best fit is with $p^* = 1 \times 10^5 \text{ Nm}^{-1}$.

Tuning the Ice Model

The previous parameter study shows that the average power input to the ice from the atmosphere P_a and the power input to the ocean P_w provide quantitative measures for verifying model performance. These variables help describe how well the velocity and deformation fields fit observed values. The two calculations that most closely approximate the power inputs are Runs 3H and I.

Although the ideal plastic ice model just described is used to simulate a few days of ice behavior accurately, there are cases where it must be inaccurate. When a region undergoes large deformations (either opening or closing), changes in the thickness distribution (production or depletion of open water and thin ice) must change the yield strength locally. If this softening or hardening is ignored, as in an ideal plastic model, then subsequent response can be in serious error. With this in mind, the remainder of this work uses results of a model that

allows hardening/softening behavior. Strength changes depend on thickness distribution changes. This concept is an important physical feature of the AIDJEX model (Coon et al., 1974). Recently, a modified formulation has allowed this hardening behavior to be included in a model that has strength on the order of 10^5 Nm^{-1} (Coon, et al., 1978). Such strengths were not compatible with physical definitions of material constants in the original AIDJEX model. This final version of the AIDJEX model includes a shear energy sink that treats energy dissipation without redistribution of ice. This generalization and a redefinition of material constants increase the initial yield strength to $1 \times 10^5 \text{ Nm}$ and also prohibit softening in many shearing situations where the previous model allowed it. In addition, thickness distribution has been modified to represent the latest keel depth distributions measured by the U.S.S. Gurnard upward-looking sonar in April 1976 (Wadhams, 1978). These values are extrapolated into the January-February 1976 time frame using the AIDJEX redistribution model. Our estimate of actual ice conditions were presented by Coon et al. (1978).

Understanding the Winter Energy Budget in the Beaufort Sea

In this section the energy budget for the hardening, plastic ice model with tuned parameters is studied. Particular interest is given to modification of the rate of energy transmitted into the ocean and to the horizontal transfer of energy by the ice stress.

As discussed in the Section on test conditions, two storms passed through the Beaufort Sea during the 17 day interval (Figure 6). The first storm reached a maximum during January 30, and the second storm reached a maximum during February 7 and 8. Time histories of P_a and P_w provide a vivid picture of the intensity of these storms.

The power input from the atmosphere to the ice P_a is determined from the winds and motions for the triangles in Figure 1. The power to the ocean P_w is determined from the motion and ocean stress model. Figure 7 shows the P_a and P_w calculated from a run (Run 5C) of the tuned hardening/softening model. Comparing Figure 6 and 7 it can be seen that these two terms are approximated very well. Figure 7 also shows a curve for $P_a + P_f$ when P_f is the rate at which energy comes in to or out of the region from the ice to the North and West of the region. It is the combination of $P_a + P_f$ that is available to deform the ice and go into the ocean. On January 30, $P_a + P_f$ is less than P_a and energy is leaving the region. During the storm of February 7 and 8 energy is coming into the region. On February 6 $P_a + P_f$ is greater than P_{afd} and therefore more energy is coming into the region than would be available in the region for a free drift (no strength) ice condition. The difference between curves $P_a + P_f$ and P_w is the power that is dissipated by the ice. We select January 30 and February 7 for further study of the spatial distribution of the various power density measures in this work.

The power available from the atmosphere is expressed in terms of the free drift power density, and may be seen in Figure 8 for January 30. It is seen that the maximum power available is located approximately 300 km north of the barrier islands off the north slope of Alaska, and small amounts of energy are available locally along the north slope. The circular contours represent constant levels of wind speed, and are approximately proportional to the cube of the wind speed. The wind field is not directly influenced by presence of the land mass. Air stress vectors are also shown on Figure 8. The maximum power density available is 60 mW/m^2 , the power density near the shore ranges from $10\text{--}20 \text{ mW/m}^2$.

The actual power input from the atmosphere is shown in Figure 9 where wind and buoy motions are used in the calculation. Data points at each buoy are shown. There is no power input along the north slope because the ice is stationary. The largest input power is 55 mW/m^2 . The location of the fast ice region is outlined by the dashed line. Small variations shoreward of the dashed line are ignored in drawing contours. When the same air stress field is used as input to the model simulation, the resulting velocity field provides the actual power input to the ice as shown in Figure 10 for January 30. It is seen that the same elliptical pattern of contours remains and the observed field is approximated reasonably well. The maximum power density input to the ice at this time is 30 mW/m^2 with a minimum along shore similar to that available in the atmosphere and on the order of 10 mW/m^2 .

The measured power transmitted to the ocean on January 30 is shown in Figure 11. This power is calculated using buoy motion and the water stress model. The amount of power p_w calculated by the ice model that is transferred into the ocean from the ice cover is shown in Figure 12

for January 30. This compares within 5 mW/m^2 with the measured values of Figure 11. The magnitudes are dramatically smaller than that input into the ice from the atmosphere. Maximum values input are in the order of 10 mW/m^2 with almost the entire study area receiving less than 5 mW/m^2 . The power input to the ocean from the ice is proportional to the cube of the ice speed if we ignore geostrophic ocean currents. The superposed velocity field indicates larger speeds in the western portion of the basin and smaller speeds in the eastern region that has just begun to move and these variations are reflected in the contours of Figure 11.

The difference between power input from the atmosphere and that transmitted into the ocean is $p_i = p_a - p_w$. This power represents the effect of ice stress. On January 30 it is shown in Figure 13. Since the p_a term is much larger than p_w Figure 13 tends to look very similar to the power from the atmosphere (Figure 10). It is seen that the largest power input to the ice is in the middle of the region and is in the order of 30 mW/m^2 . Small values are input locally near the edges of the basin.

This power input to the ice p_i may be decomposed into the power dissipated by deformation p_d and the divergence of the stress flux p_f . The power from the divergence of the stress flux is shown in Figure 14. In this figure there are both negative and positive contours. A negative value shows that energy is leaving the point and a positive value shows that energy is coming into the point through the ice cover. The area integral of the power from the divergence of the stress flux on January 30 must be negative. This is shown in Figure 7, which presents the average power over the region. At this time energy is leaving the

region at the west boundary with the stress in compression and the motion of the ice to the west. The high positive values of contours along the north slope show that a large amount of energy is coming into that area.

The stress power or power dissipated by deformation p_d on January 30 is shown in Figure 15. In contrast to the power input locally to the ice by the difference between atmosphere and ocean terms, the power dissipated by the ice cover is concentrated along the shorelines. In the central Arctic regions, it is seen that dissipation by the ice cover is zero (this term cannot be less than zero) whereas along the shorelines, a maximum on the order of 100 mW/m^2 is obtained. These large values occur when large deformations along shorelines and large stresses exist simultaneously. In Figure 15 dissipation in the vicinity of 75° North and 130° West is introduced by spurious motion of the boundary buoy and should be ignored. However, the concentration of large amounts of dissipation along the north slope of Alaska is physically real. The band of shearing that causes this large energy dissipation is seen to be approximately 150 km wide and covers approximately three cells in the numerical grid. For the calculation discussed in this work the maximum dissipation occurs at the shoreline. Qualitatively this result is quite acceptable. However, other simulations (Pritchard, 1977) have shown that the flaw lead existed at this time approximately 150 km offshore. Quantitatively, therefore, one should expect that there is very little energy dissipated shoreward of this 150 km line, and the concentrations seen in Figure 15 should be moved out to the location of the flaw lead. It is known from previous parameter studies that this offshore flaw lead is modeled accurately when strengths are increased to the order of

1.5×10^5 Nm . Those higher strength values are also consistent with results of the parameter study discussed earlier in this work. It is seen that the power available from the atmosphere p_a and input to the ice p_i over the entire Beaufort Sea (Figures 10 and 13) is transferred by the stress in the ice cover and dissipated over the Continental Shelf. This physical process of a horizontal energy transfer is different from open oceans and appears to be an important process in ice covered oceans. It is a mechanism that controls the dissipation of marine energy over the shelf regions in polar oceans. It should be pointed out that along the eastern shore of the region, near Banks Island, the power dissipated by the ice cover is negligible even though deformations in that region are large. The opening of a lead along the land is occurring. The small power dissipation occurs because stresses are negligible in that opening region.

If the generation of acoustic energy by ice ridging is of concern, the power dissipation contours can be used to determine where energy is being dissipated by the ice cover. It is easy to imagine that the energy dissipated by deformation will create noise and much of this noise will be transmitted into the ocean and propagated from that point. Operators in the Beaufort Sea should well suspect that on January 30 conditions over the Continental Shelf along north slope of Alaska would be quite noisy. By the same token, one should expect relatively little contribution to the noise level from the area near Banks Island.

The conditions described in Figures 8-15 are easterly winds and ice velocities toward the west. Large shearing deformations along the north slope of Alaska and uniaxial opening along the shoreline of Banks Island typically occur under these conditions. In the next sequence of figures,

conditions where ice drift and winds are towards the McKenzie delta and Banks Island are presented. These create convergence in the Canadian Beaufort Sea. At the same time shearing occurs along the Alaskan north slope but the shearing is in the opposite sense compared with previous days. The power available from the atmosphere at this time is shown in Figure 16 for February 7. For this case, contour levels run approximately from the southwest to the northeast, with maximum winds to the north of Barter Island. The power available at this time is a maximum of approximately 30 mW/m^2 . The average power available over the entire region of interest is approximately 27 mW/m^2 .

The observed p_a is shown in Figure 17 and the p_a from the model calculation are shown in Figure 18. The power input to the ice from the atmosphere on February 7 is affected significantly by the presence of the land mass. (Compare Figures 16 and 17.) Contours are seen to generally follow the shape of the north slope of Alaska and Canada. Maximum values input to the ice from the atmosphere according to this simulation are on the order of 20 mW/m^2 . Since the ice is assumed to be at rest at the shore, one must always expect zero input at this point because of the zero velocity. The exception to this case arises, of course, when a velocity discontinuity appears at the shoreline, but the numerical solution scheme does not represent such discontinuities.

The measured p_w is shown in Figure 19 and the p_w from the model calculation is shown in Figure 20. The power input to the ocean on February 7 is small throughout the region of interest. Except at the extreme northwest boundary, power throughout the area is 5 mW/m^2 or less. The small values occur because the velocity throughout the region is small as seen in the superposed ice drift vectors (Figure 20). The

velocity field is small in magnitude at this time because onshore winds during the last day have caused convergence of the ice cover along the eastern shore and the material has hardened. Hardening of the ice model allows an increase in stress levels which prevents further motion.

The effect of the ice for February 7 is shown in Figure 21 with contours from $5-15 \text{ mW/m}^2$. The effect of the ice is uniform over the region. However, when p_i is decomposed into p_f and p_d this view changes. The power from the divergence of the stress flux on February 7 is shown in Figure 22. Here again, both negative and positive contours occur. However, there is a net energy input to the region as can be seen from Figure 7. The areas along the north slope and along the Canadian Archipelago show that large amounts of energy are being transferred to these areas.

Power dissipated by the ice cover on February 7 is presented in Figure 23. As usual, it is concentrated around the shorelines. Along the north slope of Alaska a strong shearing occurs as the ice moves toward the east with local power dissipation on the order of 80 mW/m^2 . These values fall rapidly within the first 75 km from shore. Along Banks Island and Tuktoyaktuk Peninsula the convergence again creates large values of dissipation. Maximum local values occur across Amundsen Gulf and reach a magnitude of 50 mW/m^2 . In this region of uniaxial convergence, contours are spread wider spatially than they are in the region of shear along the Alaskan north slope. This spreading is caused by hardening that occurs in compression. As the material hardens, dissipation occurs throughout the region of hardening. In contrast, shearing occurs with little change in yield strength, and therefore deformations are concentrated either along discontinuities or narrow

regions. During February 7 one could expect that the power dissipated by deformation of the ice cover would create noise along both the Alaskan north slope and the Canadian Archipelago.

Conclusion

The mechanical energy variables considered in this work provide useful measures of comparison between modeled and observed sea ice behavior. The power input to the ice cover from the atmosphere is useful for determining when strong storms or interesting extreme events occur.

If barometric pressure fields (or wind fields) and ice motion data are available, the free drift power available from the atmosphere, the actual power input to the ice from the atmosphere and the power input to the ocean can be found. Although useful, these variables are inadequate for estimating other important terms in the mechanical energy budget.

To determine the mechanical energy budget completely requires an ice model or constitutive law. With this model, knowledge of the ice stress allows stress flux divergence and energy dissipation by the ice to be evaluated. The stress flux divergence is needed to determine how energy is transferred horizontally through the ice cover and explains the fact that energy is dissipated primarily around the margins of the ice-covered oceans. These processes should be helpful in interpreting how coastal erosion is altered by the ice cover and how acoustic energy is generated in these areas.

A comparison of energy input to the ice from the atmosphere and of the energy transferred to the ocean has allowed a plastic sea ice model to be tuned. We have first of all shown that these energy measures are useful for model tuning and have then used the results. A diamond shape yield surface is seen to be better than the teardrop used previously. A yield strength of $1 \times 10^5 \text{ Nm}^{-1}$ is judged best. However, this is slightly different from the value of $1.5 \times 10^5 \text{ Nm}^{-1}$ that would be chosen by

considering only the velocity field. Such differences point out the importance of comparing all quantities of interest rather than just one. It is now felt that yield strength and yield surface shape are defined well enough that further work must consider many more physical processes simultaneously. These include anisotropy, tensile strength, ice age, floe size and scale effects.

Results of the model calculation during the seventeen day test period show that a variety of conditions can arise. We have found times when energy is increased in the Beaufort Sea from distant regions and other times when it is decreased. At times these boundary effects are large enough so that power input even exceeds maximum power available from the atmosphere over the Beaufort Sea.

Acknowledgement

This work was supported by the Office of Naval Research through
Contract Number N00014-79-C-0147.

References

- Coon, M. D., Maykut, G. A., Pritchard, R. S., Rothrock, D. A. and Thorndike, A. S. (1974) "Modeling the Pack Ice As An Elastic-Plastic Material," AIDJEX Bulletin, No. 24, The University of Washington, Seattle, Washington, pp. 1-106.
- Coon, M. D. and Pritchard, R. S. (1979) "Mechanical Energy Considerations in Sea Ice Dynamics," J. Glaciology, Vol. 24, No. 90, pp.
- Coon, M. D., Pritchard, R. S. and Leavitt, E. (1978) AIDJEX Modeling Grant Final Report to National Science Foundation.
- Holland, W. R. (1978) "The Role of Mesoscale Eddies in the General Circulation of the Ocean-Numerical Experiments Using a Wind-Driven Quasi-Geostrophic Model," J. Physical. Oceanography, Vol. 8(3), pp. 363-392.
- Maykut, G. A. and Untersteiner, N. (1971) "Some Results From a Time-Dependent Thermodynamic Model of Sea Ice," Journal of Geophysical Research, 76, pp. 1550-1575.
- Pritchard, R. S. (1975) "An Elastic-Plastic Constitutive Law for Sea Ice," J. Appl. Mech., 42(2), pp. 379-384.
- Pritchard, R. S. (1977) "The Effect of Strength on Simulations of Sea Ice Dynamics," POAC 77 Proceedings, Vol. I, eds. D. B. Muggeridge and G. R. Peters, Ocean Engineering Information Centre, Memorial University of Newfoundland, St. John's, pp. 494-505.

References (Cont.)

Pritchard, R. S., Coon, M. D. McPhee, M. G. and Leavitt, E. (1977)

"Winter Ice Dynamics in the Nearshore Beaufort Sea," in Environmental Assessment of the Alaskan Continental Shelf, Vol. XVI, Outer Continental Shelf Environmental Assessment Program, Boulder, Colorado, pp. 164-332; Also in AIDJEX Bulletin, 37, The University of Washington, Seattle, Washington, pp. 37-93.

Rothrock, D. A. (1975) "The Energetics of the Plastic Deformation of Pack Ice by Ridging," J. Geophysical Research, 80(33), pp. 4514-4519.

Thorndike, A. S., Rothrock, D. A., Maykut, G. A. and Colony, R. (1975)

"The Thickness Distribution of Sea Ice," J. Geophysical Research, 80(33), pp. 4501-4513.

List of Figures

- Figure 1. Beaufort Sea Region Subdivided into Triangles by Manned Camps and Data Buoys.
- Figure 2. Schematic of Important Terms Contributing to Mechanical Energy Budget.
- Figure 3. Yield Surface Shapes Considered in Parameter Study.
- Figure 4. Comparison of Modeled Average Atmospheric Power to Ice in Beaufort Sea for a Range of Strength and Yield Surfaces.
- Figure 5. Comparison of Modeled Power to Ocean in Beaufort Sea for a Range of Strength and Yield Surfaces.
- Figure 6. Observed Averaged Atmosphere Power to Ice and to Ocean in Beaufort Sea During Seventeen Day Test Period.
- Figure 7. Average Power Variables Calculated from the Best Model During Seventeen Day Test Period.
- Figure 8. Free Drift Power Available p_{afd} on January 30. All contour levels in mW/m^2 . Scale vector is for air stress vectors.
- Figure 9. Observed Atmospheric Power to Ice p_a on January 30. All contour levels in mW/m^2 .
- Figure 10. Modeled Atmospheric Power to Ice p_a on January 30. All contour levels in mW/m^2 .
- Figure 11. Observed Power to Ocean p_w on January 30. All contour levels in mW/m^2 .
- Figure 12. Modeled Power to Ocean p_w on January 30. All contour levels in mW/m^2 . Scale vector is for ice velocity vectors.

List of Figures (Cont.)

- Figure 13. Effect of Ice Stress p_i on January 30. All contour levels in mW/m^2 .
- Figure 14. Stress Flux Divergence p_f on January 30. All contour levels in mW/m^2 .
- Figure 15. Power Dissipated by Ice p_d on January 30. All contour levels in mW/m^2 .
- Figure 16. Free Drift Power Available p_{afd} on February 7. All contour levels in mW/m^2 . Scale vector is for air stress vectors.
- Figure 17. Observed Atmospheric Power to Ice p_a on February 7. All contour levels in mW/m^2 .
- Figure 18. Modeled Atmospheric Power to Ice p_a on February 7. All contour levels in mW/m^2 .
- Figure 19. Observed Power to Ocean p_w on February 7. All contour levels in mW/m^2 .
- Figure 20. Modeled Power to Ocean p_w on February 7. All contour levels in mW/m^2 . Scale vector is for ice velocity vectors.
- Figure 21. Effect of Ice Stress p_i on February 7. All contour levels in mW/m^2 .
- Figure 22. Stress Flux Divergence p_f on February 7. All contour levels in mW/m^2 .
- Figure 23. Power Dissipated by Ice p_d on February 7. All contour levels in mW/m^2 .

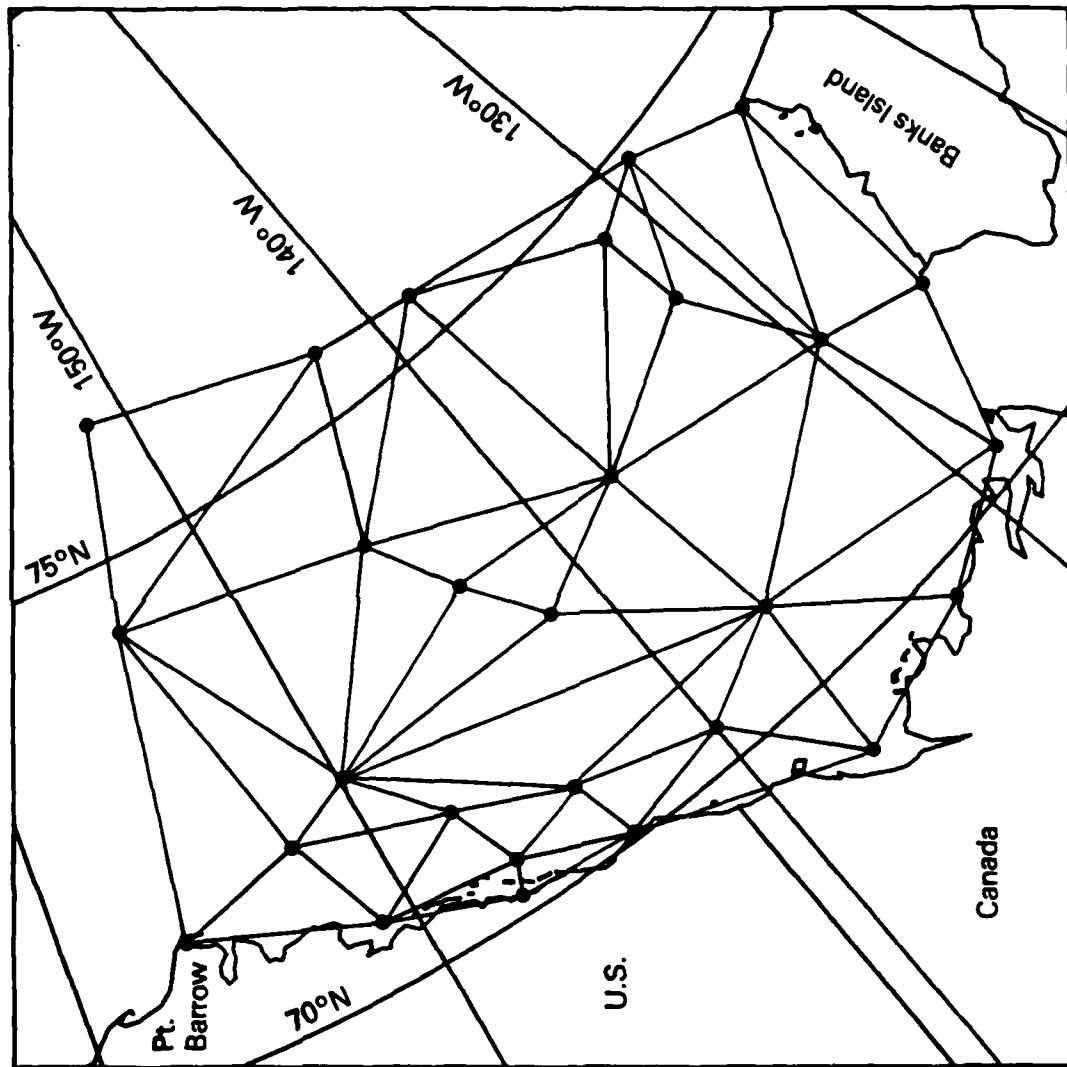


Figure 1. Beaufort Sea Region Subdivided into Triangles by Manned Camps and Data Buoys.

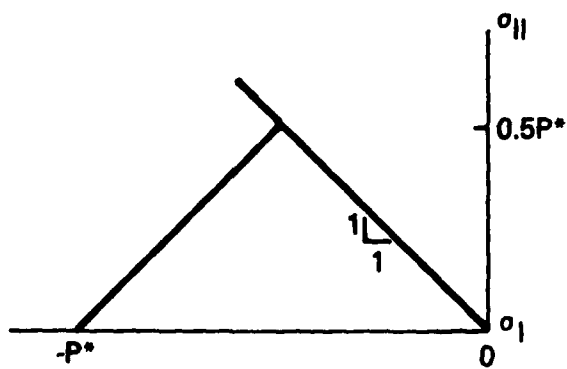
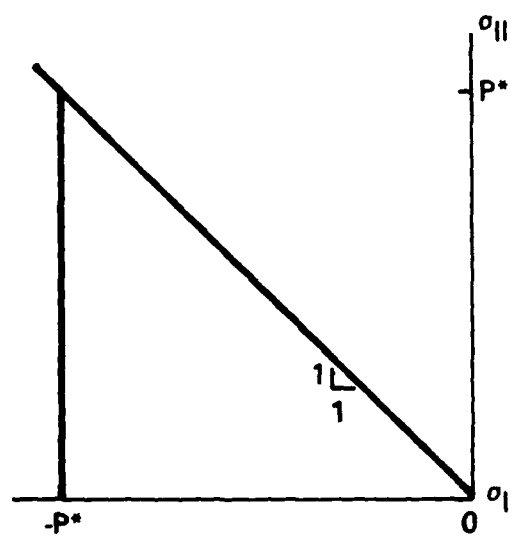
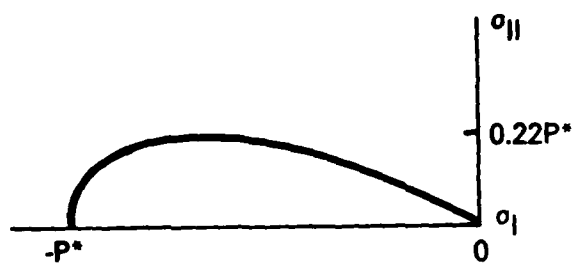


Figure 2. Yield Surface Shapes Considered in Parameter Study.

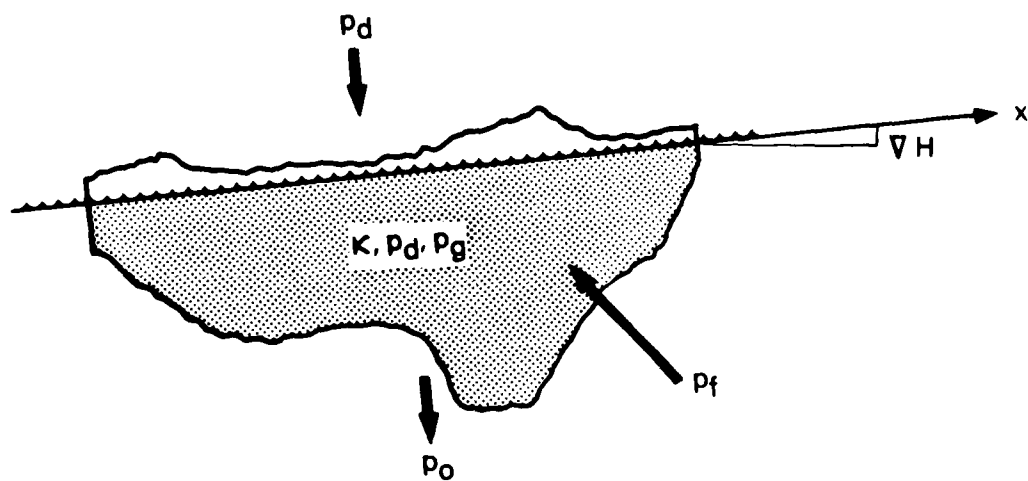


Figure 3. Schematic of Important Terms Contributing to Mechanical Energy Budget.

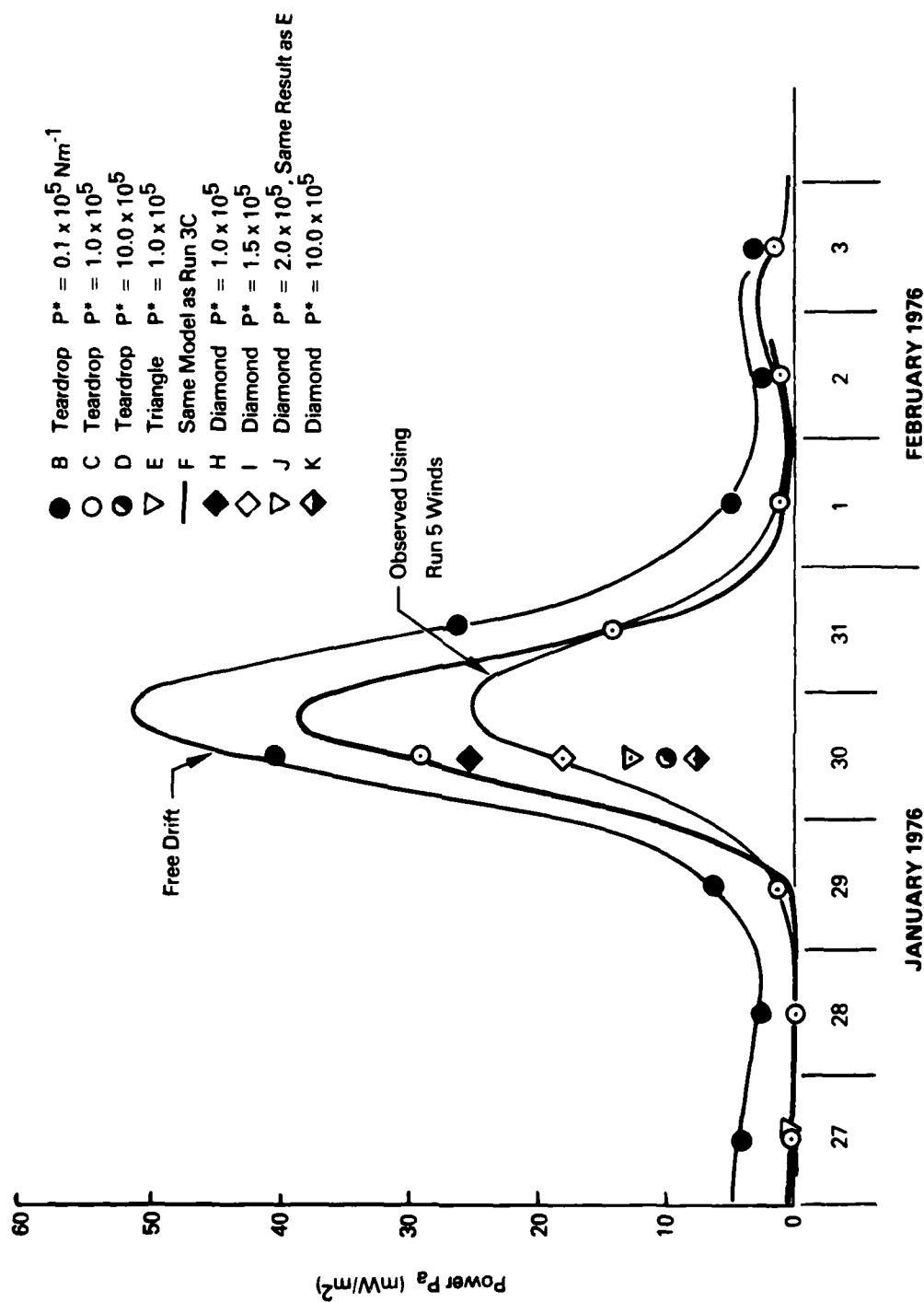


Figure 4. Comparison of Modeled Average Atmospheric Power to Ice in Beaufort Sea for a Range of Strength and Yield Surfaces.

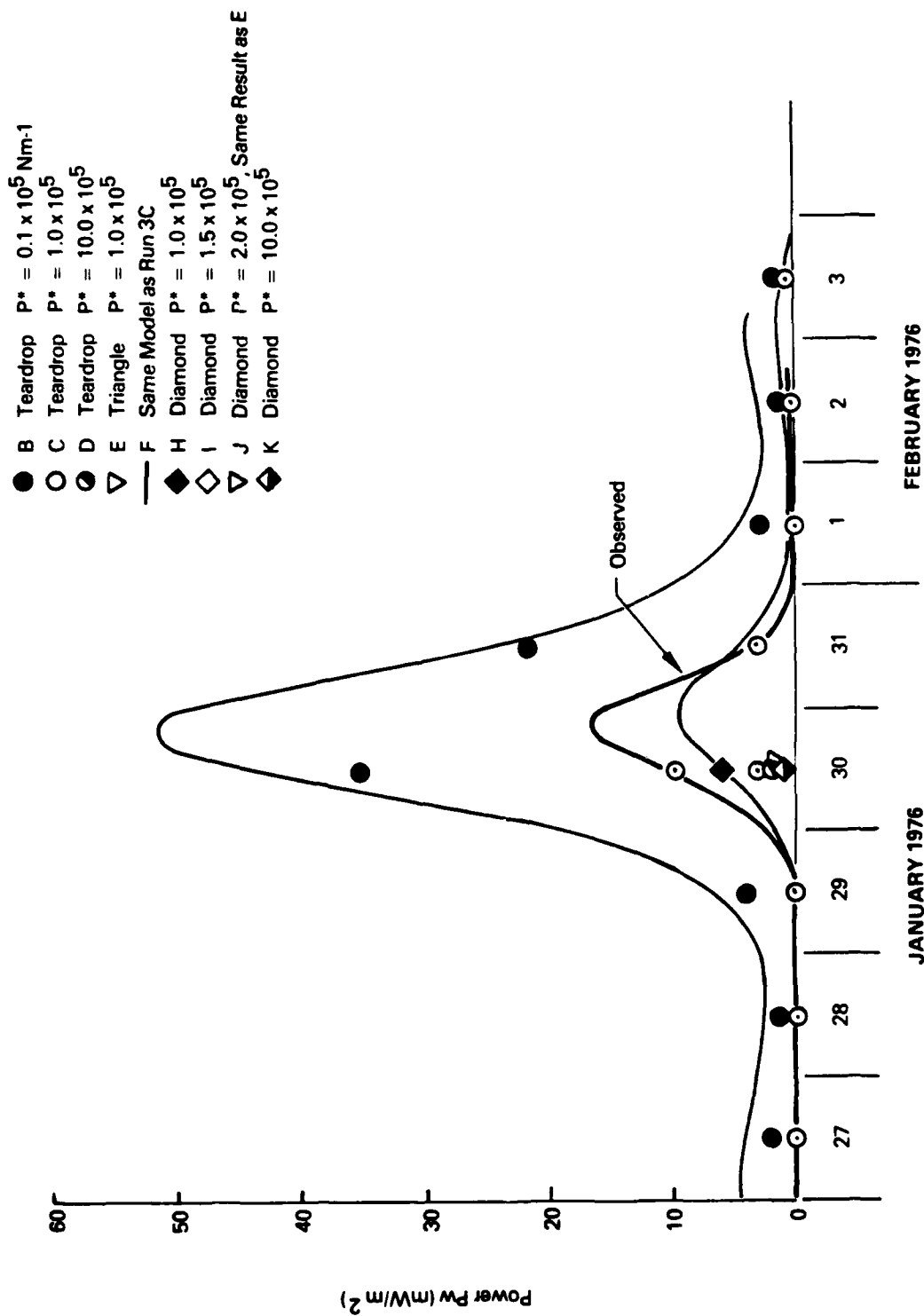


Figure 5. Comparison of Modeled Power to Ocean in Beaufort Sea for a Range of Strength and Yield Surfaces.

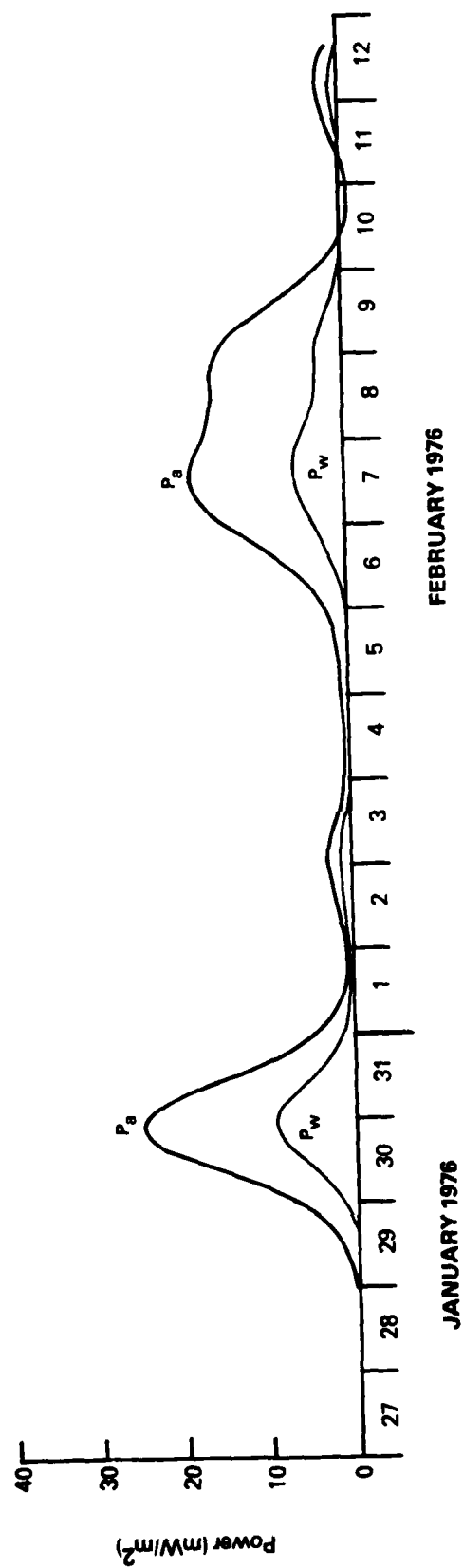


Figure 6. Observed Averaged Atmosphere Power to Ice and to Ocean in Beaufort Sea During Seventeen Day Test Period.

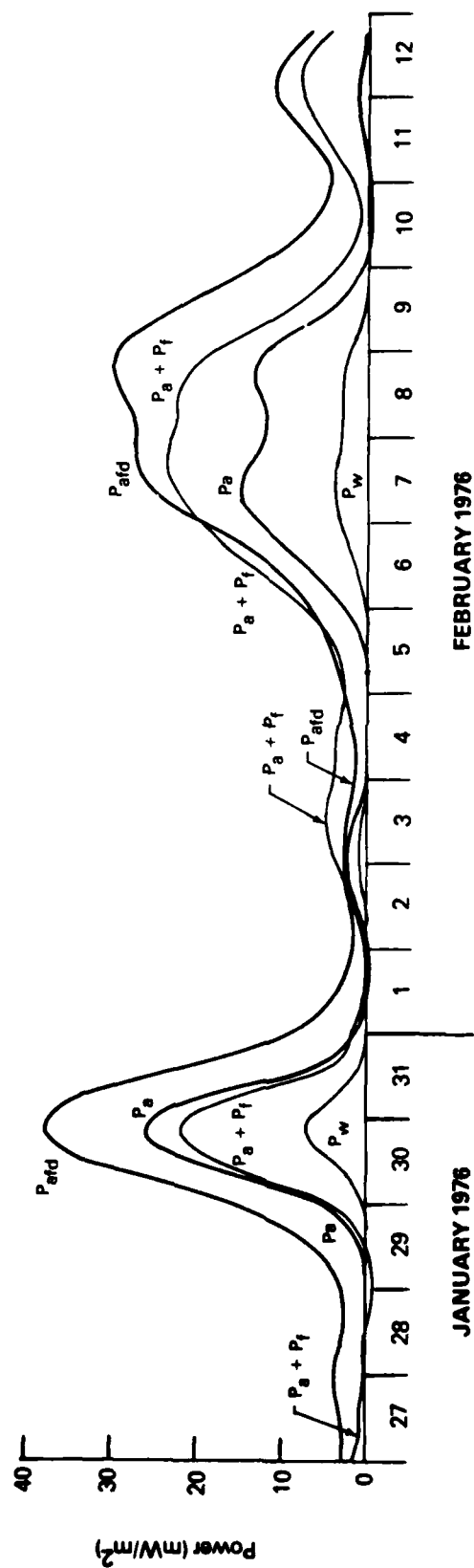


Figure 7. Average Power Variables Calculated from the Best Model During Seventeen Day Test Period.

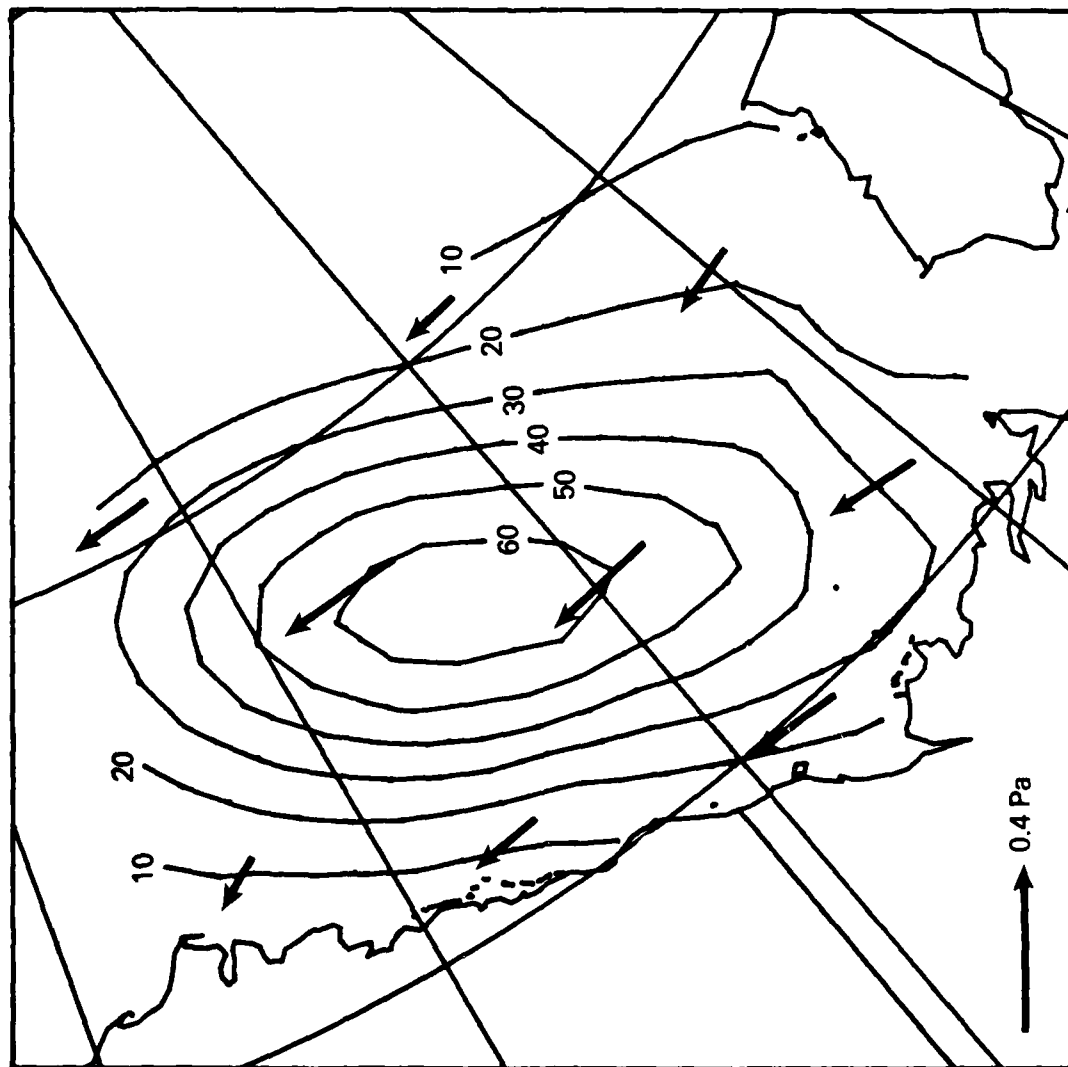


Figure 8. Free Drift Power Available p_d on January 30. All Contour Levels in mW/m^2 . Scale Vector is for Air Stress Vectors.

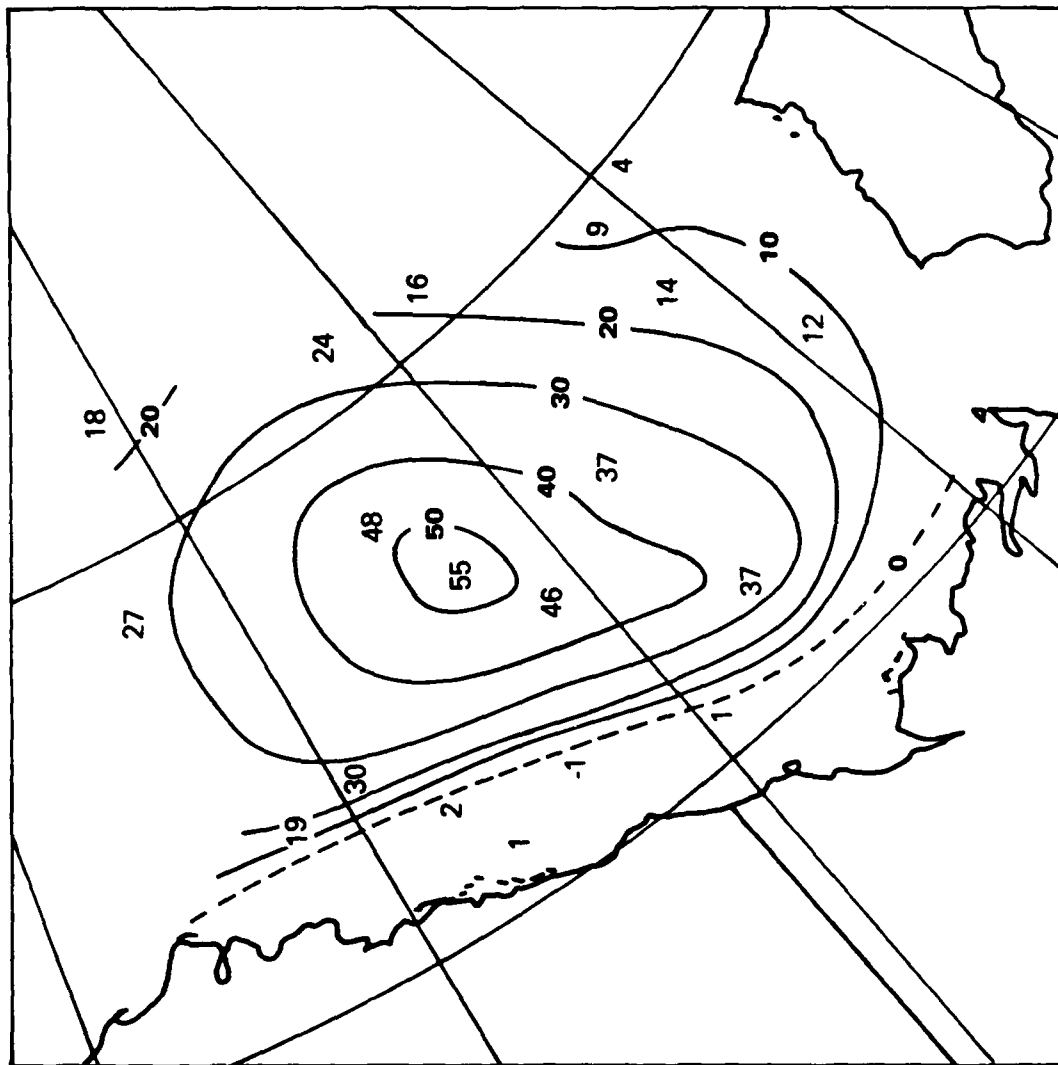


Figure 9. Observed Atmospheric Power to Ice p_a on January 30. All Contour Levels in mW/m^2 .

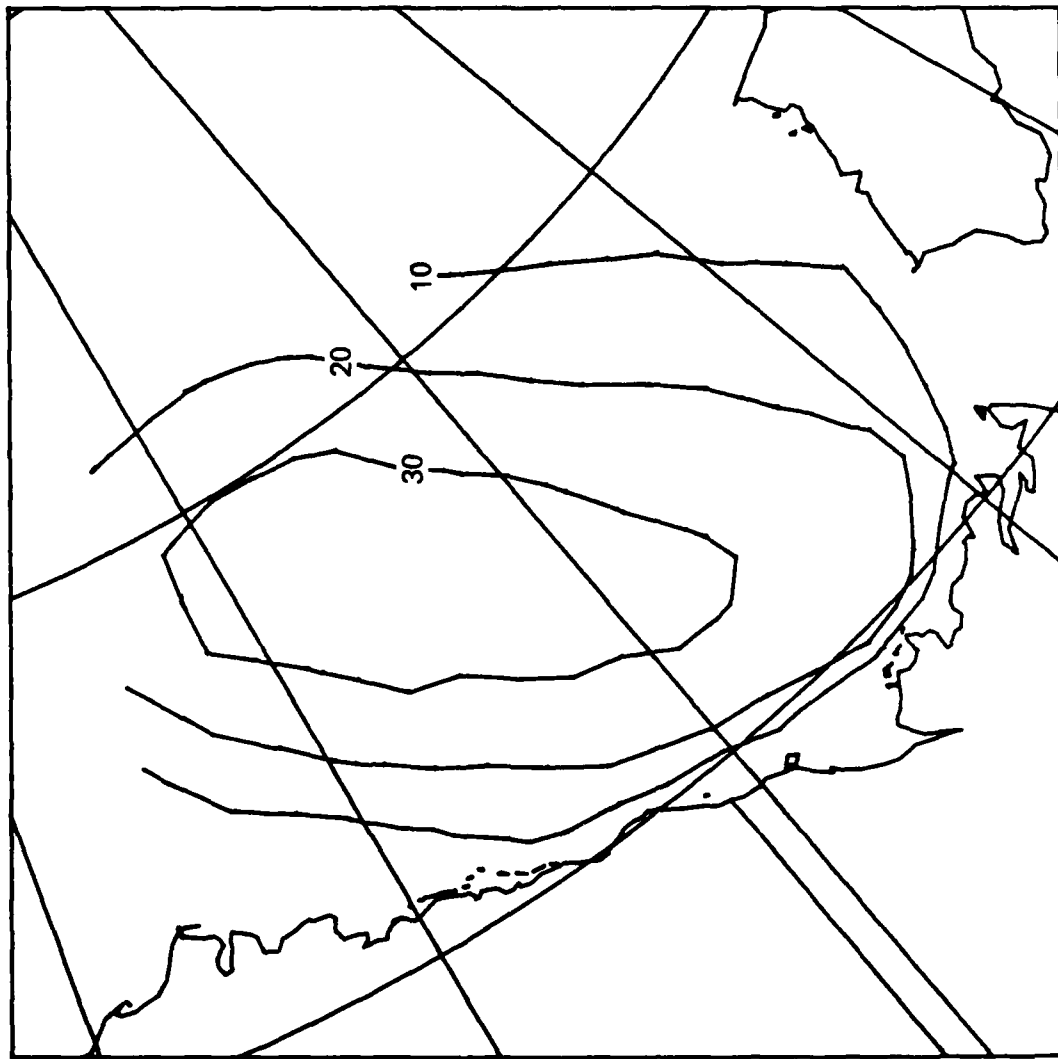


Figure 10. Modeled Atmospheric Power to Ice p_a on January 30. All Contour Levels in mW/m^2 .

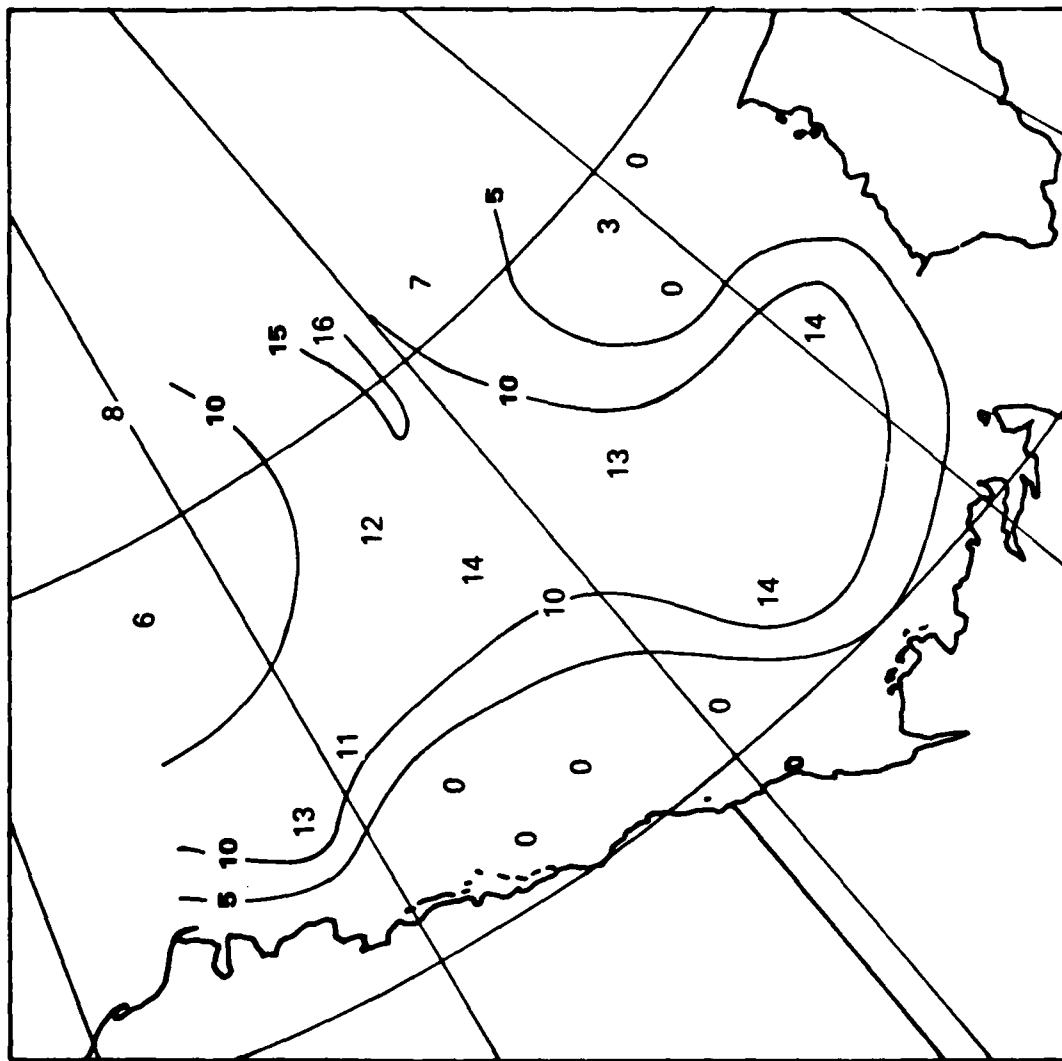


Figure 11. Observed Power to Ocean p_w on January 30. All Contour Levels in mW/m^2 .

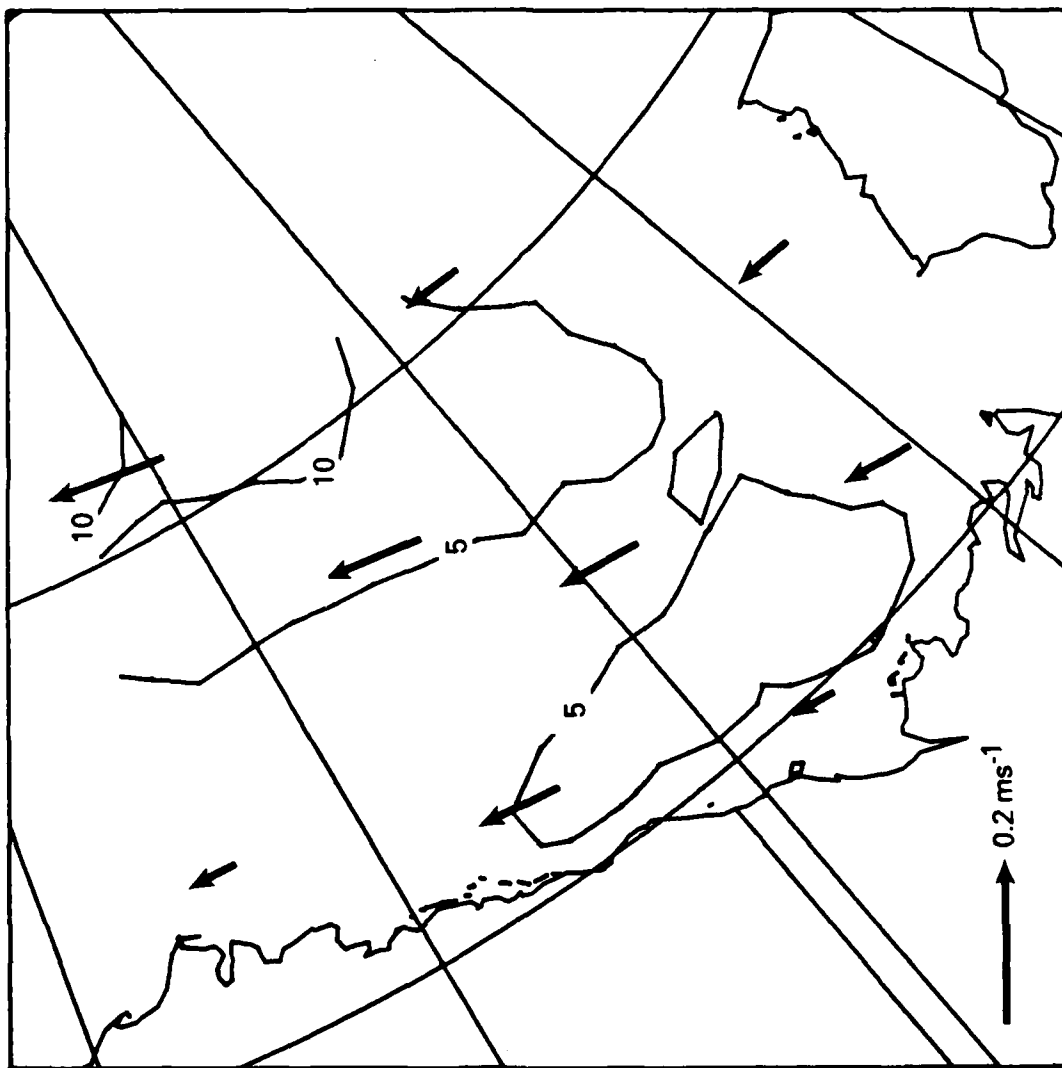


Figure 12. Modeled Power to Ocean p_w on January 30. All Contour Levels in mW/m^2 .
Scale Vector is for Ice Velocity Vectors.

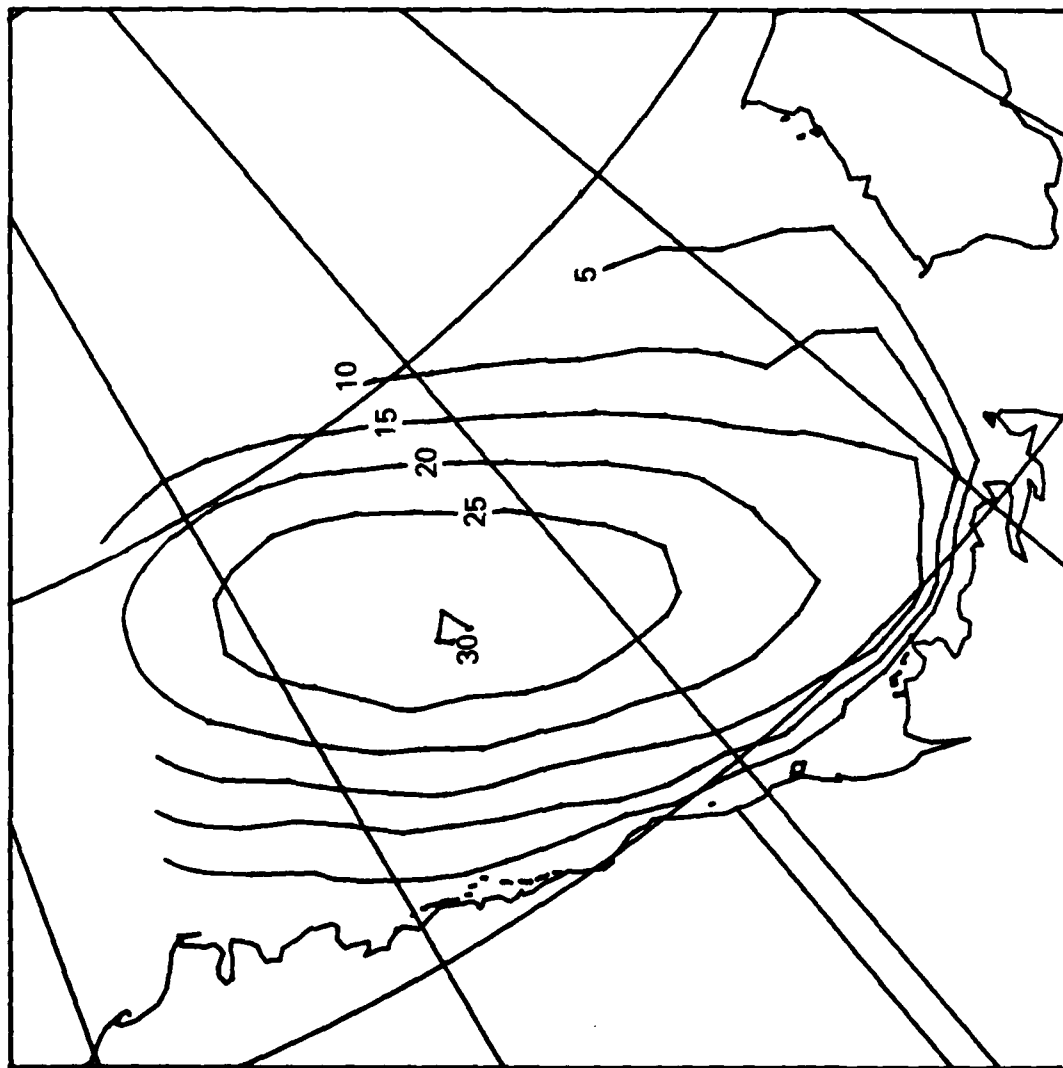


Figure 13. Effect of Ice Stress p_i on January 30. All Contour Levels in mW/m^2 .

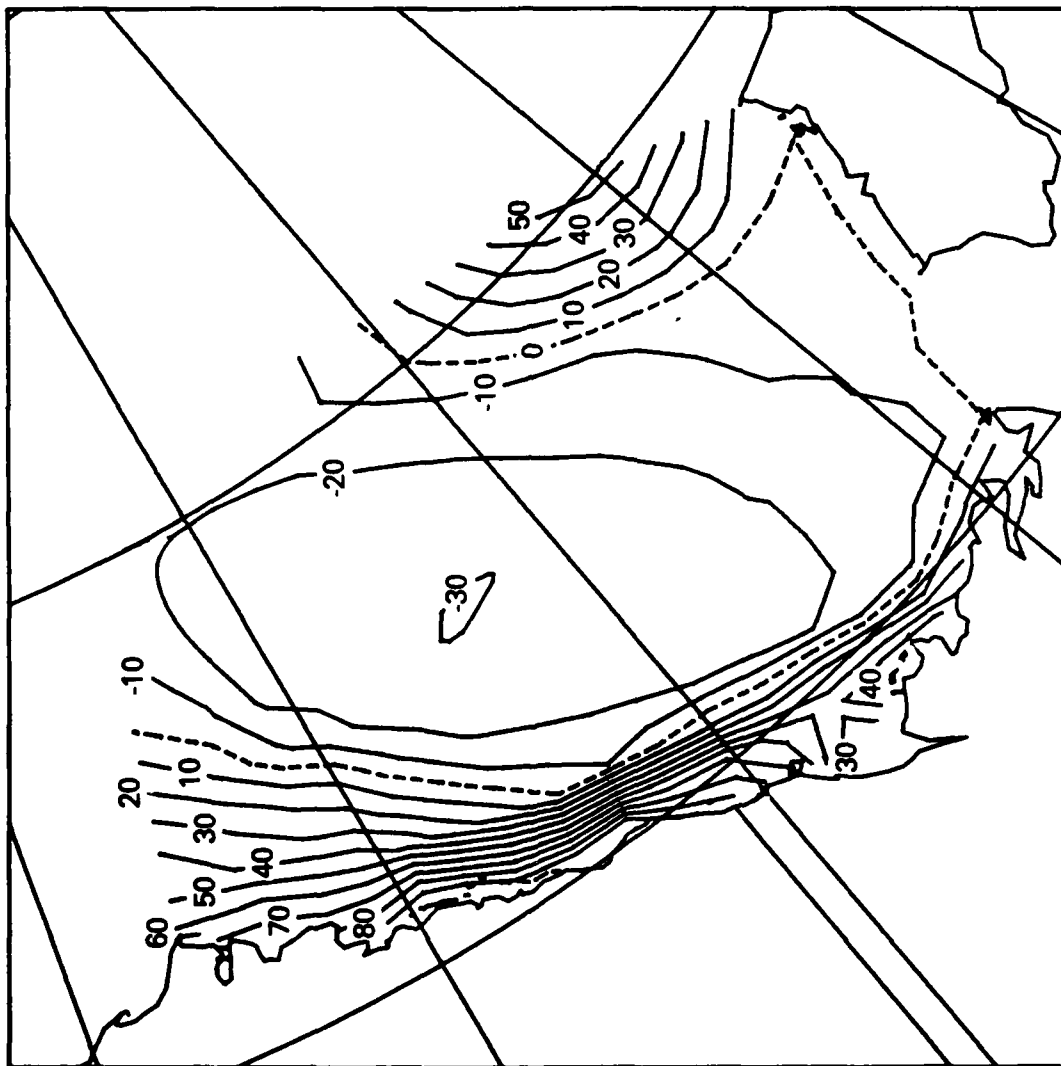


Figure 14. Stress Flux Divergence p_f on January 30. All Contour Levels in mW/m^2 .

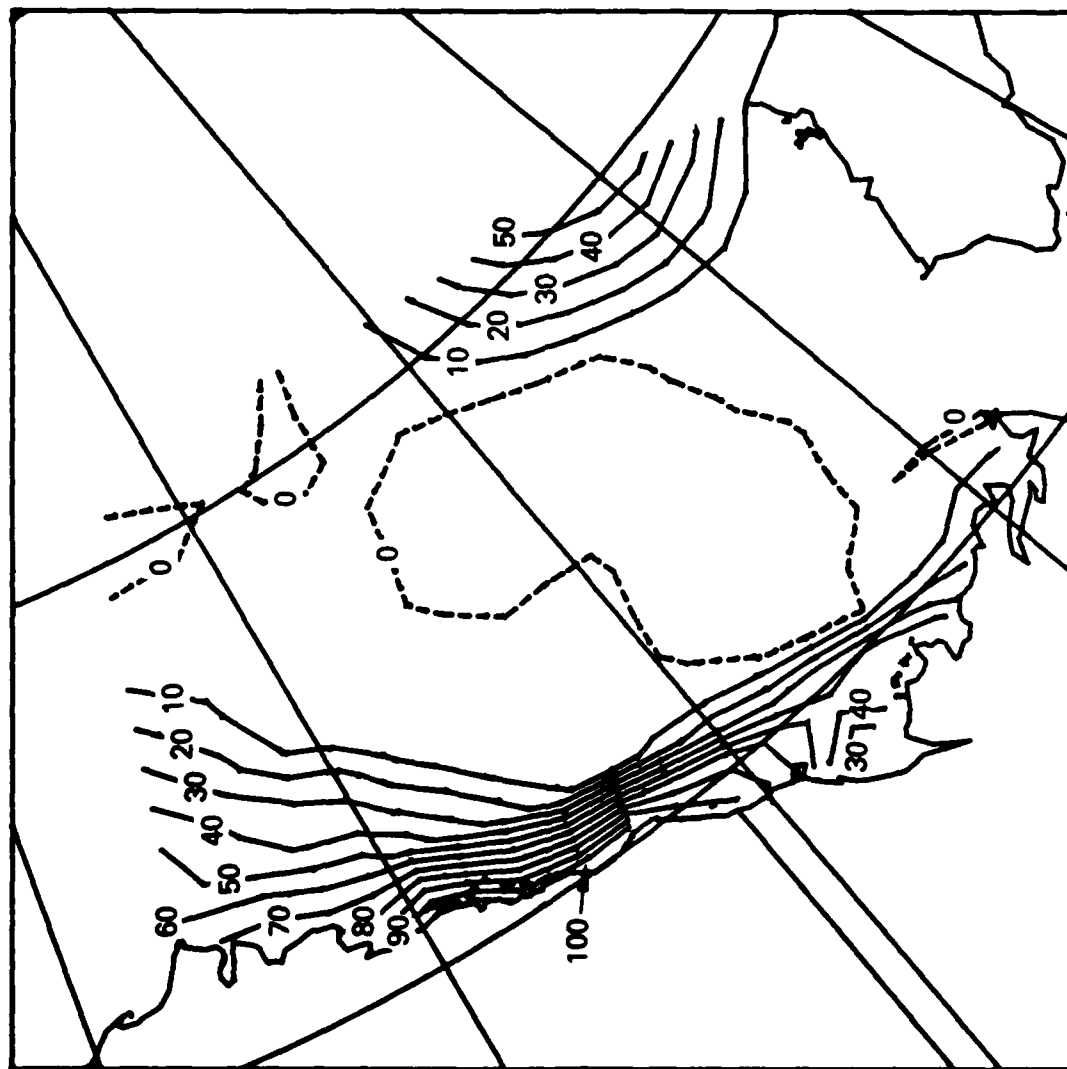


Figure 15. Power Dissipated by Ice p_d on January 30. All Contour Levels in mW/m^2 .

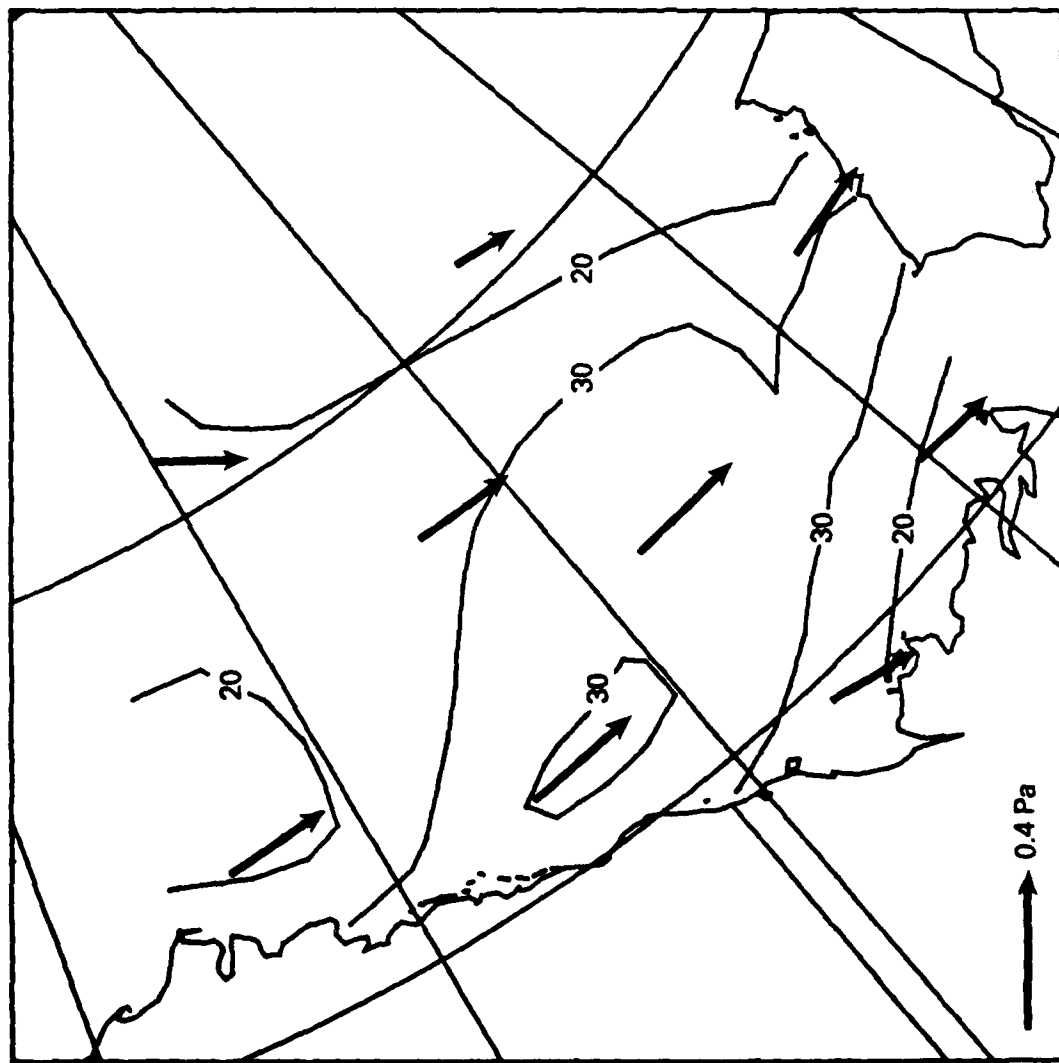


Figure 16. Free Drift Power Available p_{dfd} on February 7. All Contour Levels in mW/m^2 .
Scale Vector is for Air Stress Vectors.

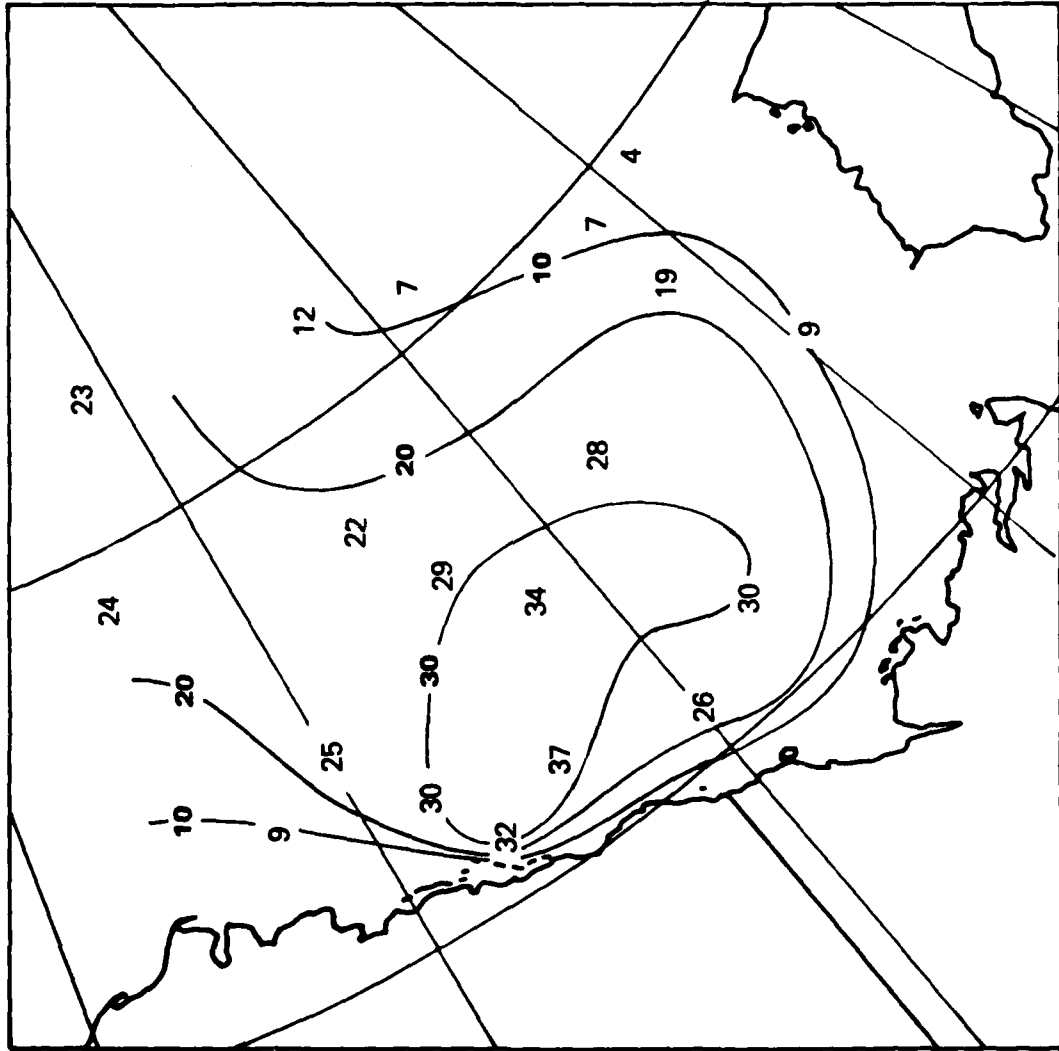


Figure 17. Observed Atmospheric Power to Ice p_a on February 7. All Contour Levels in mW/m^2 .

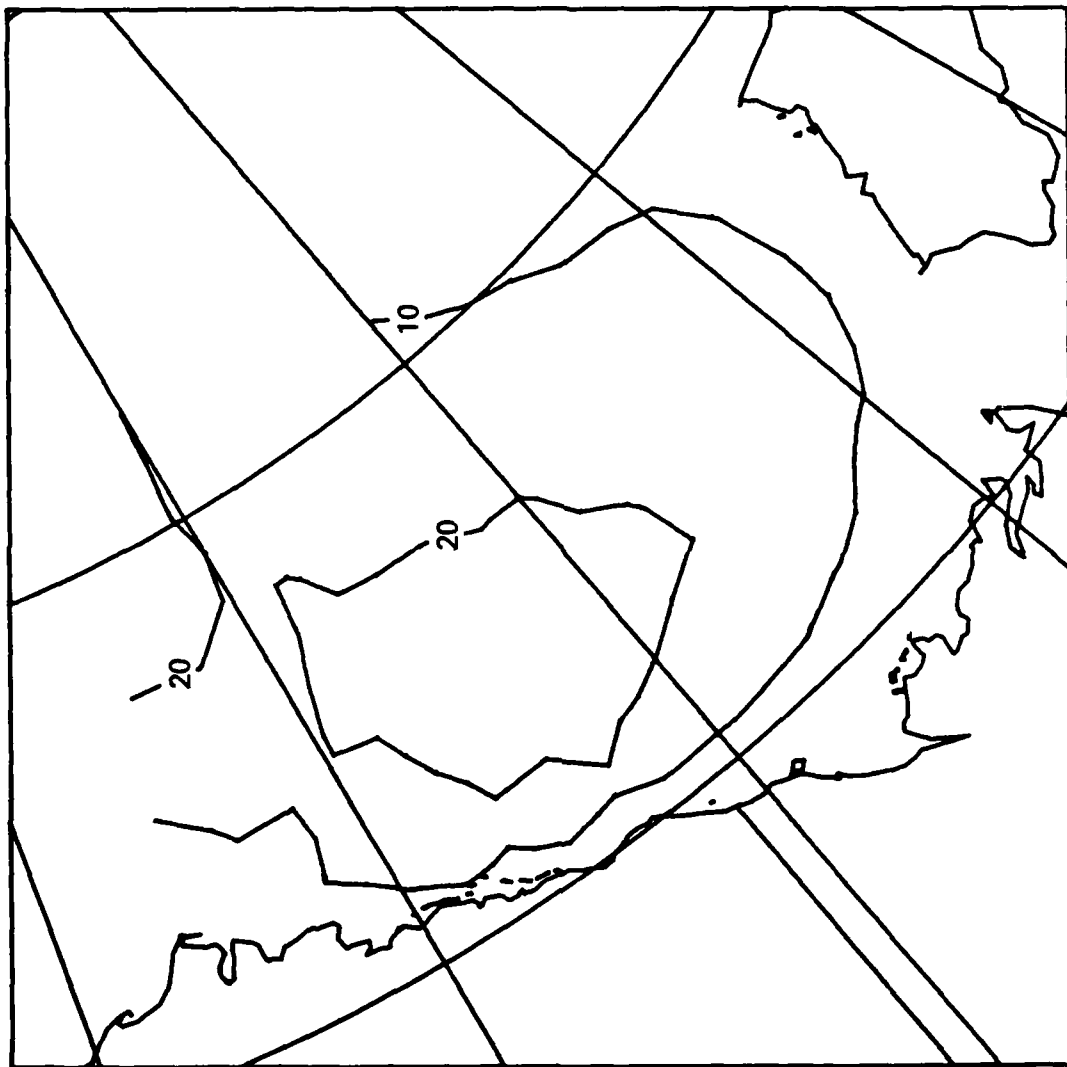


Figure 18. Modeled Atmospheric Power to Ice P_a on February 7. All Contour Levels in mW/m^2 .

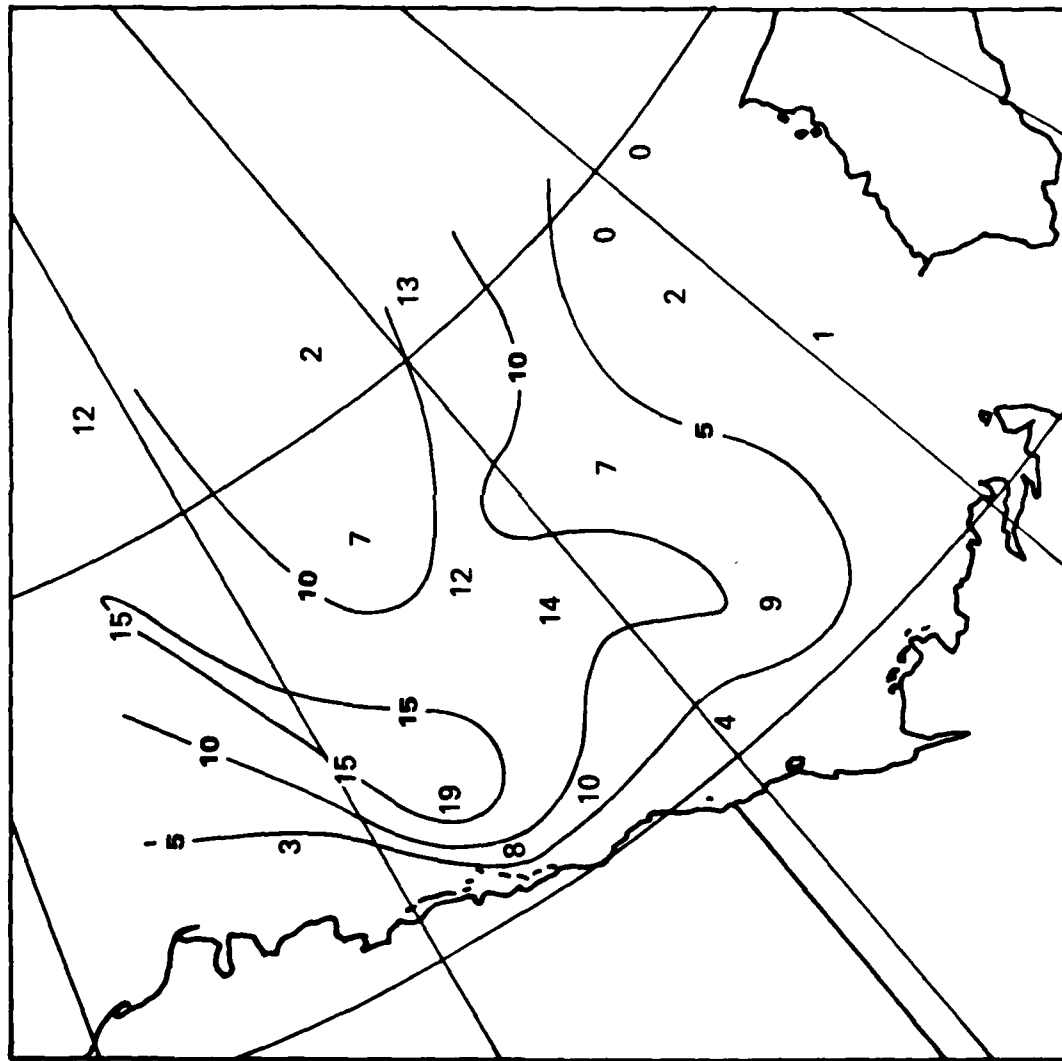


Figure 19. Observed Power to Ocean p_w on February 7. All Contour Levels in mW/m^2 .

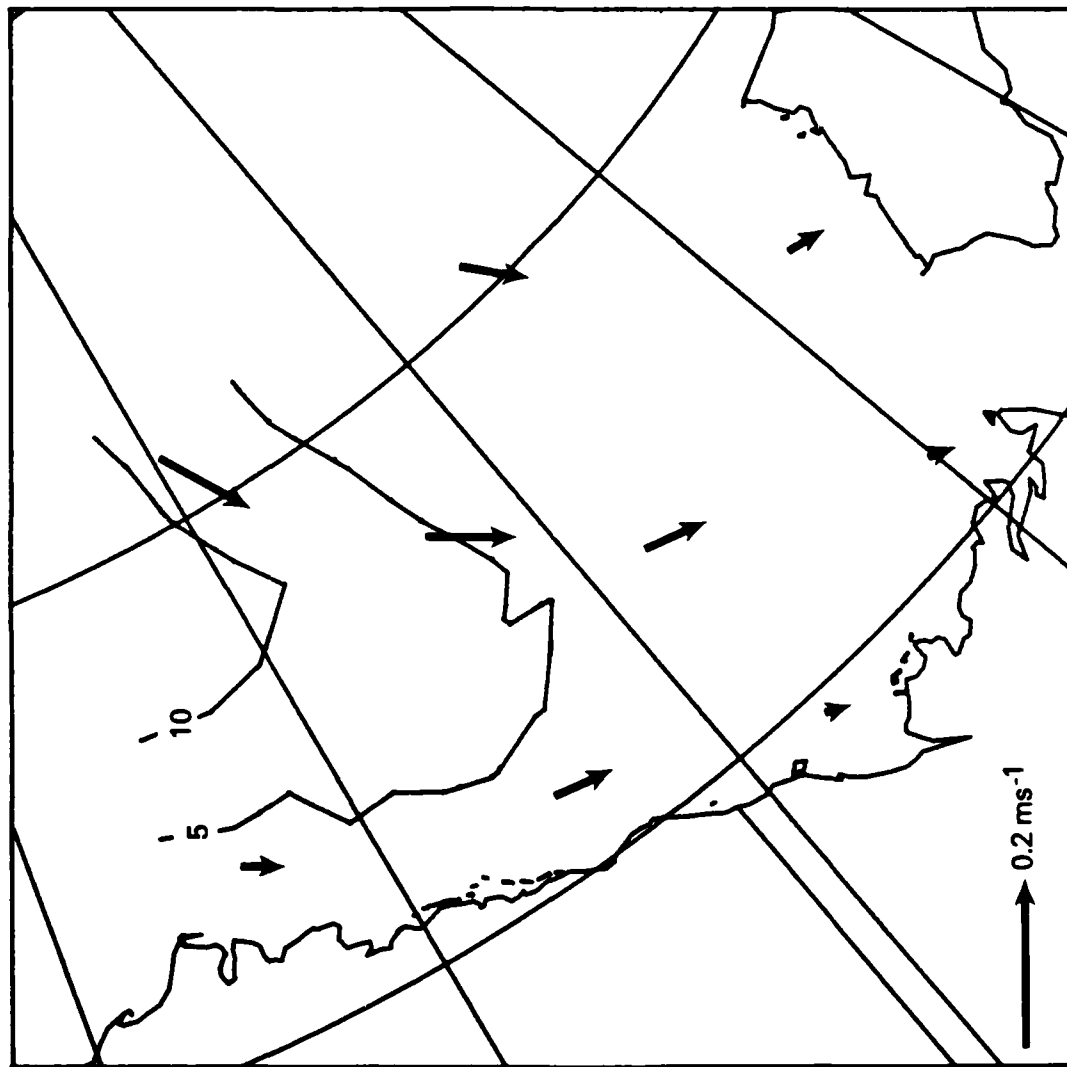


Figure 20. Modeled Power to Ocean P_w on February 7. All Contour Levels in mW/m^2 .
Scale Vector is for Ice Velocity Vectors.

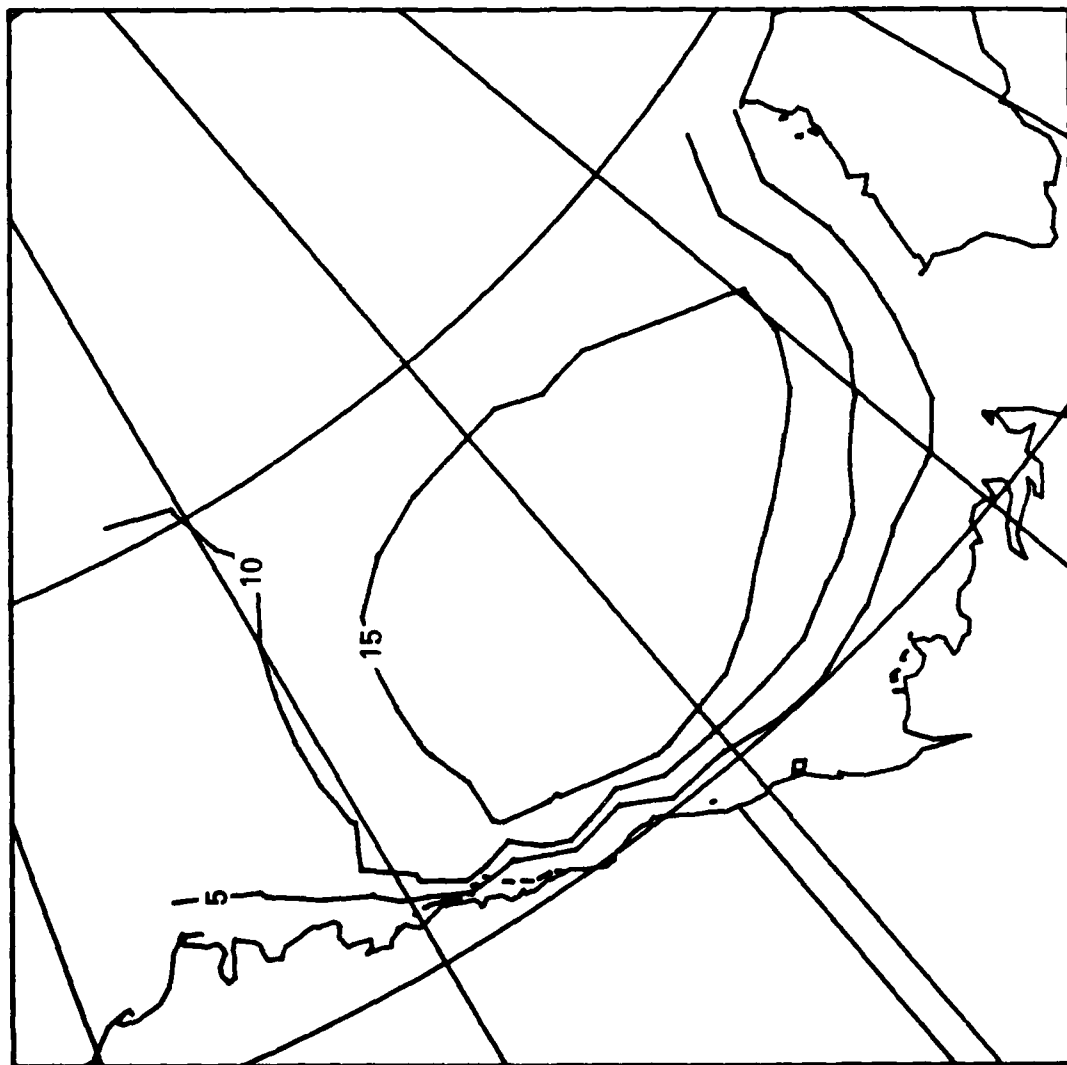


Figure 21. Effect of Ice Stress p_i on February 7. All Contour Levels in mW/m^2 .

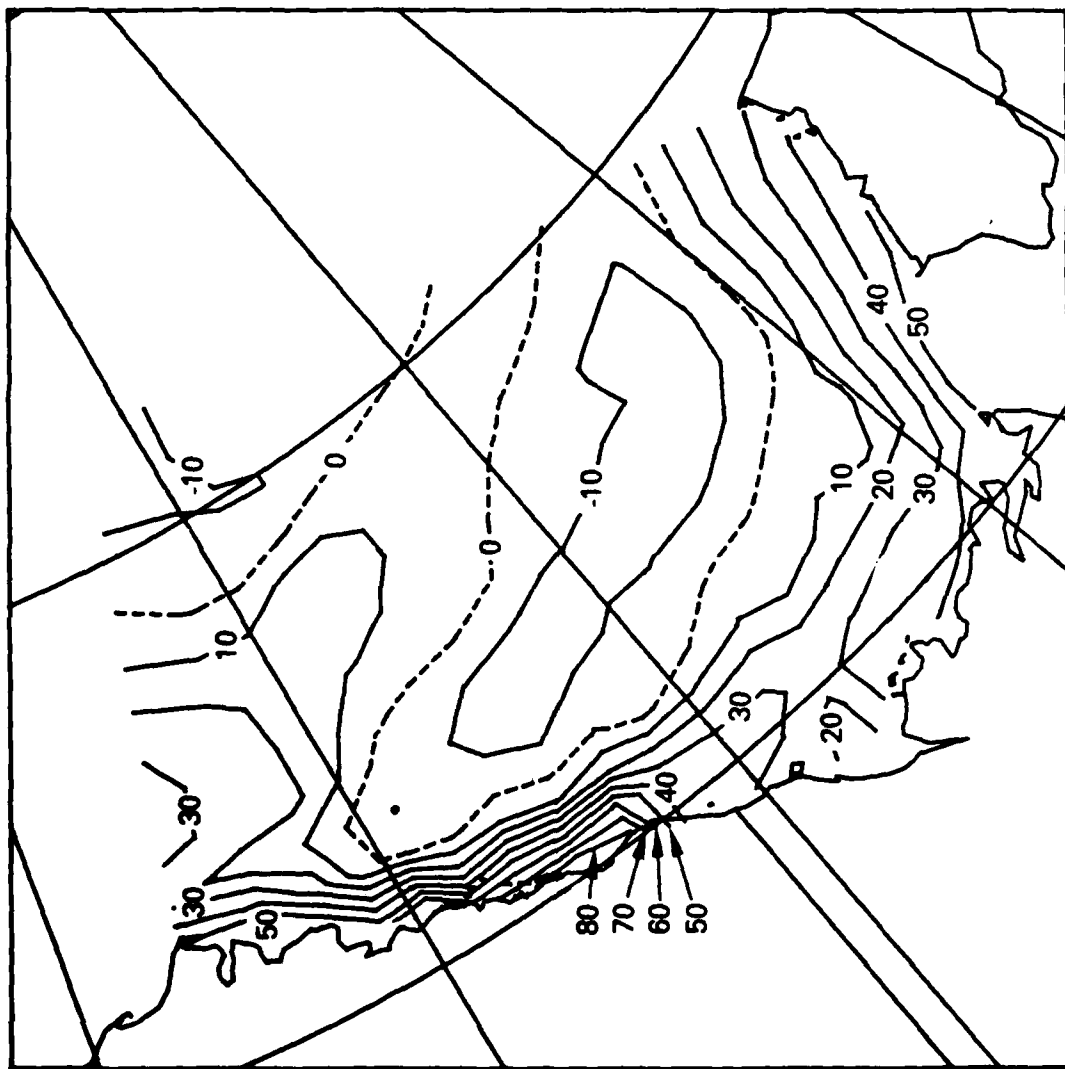


Figure 22. Stress Flux Divergence p_f on February 7. All Contour Levels in mW/m^2 .

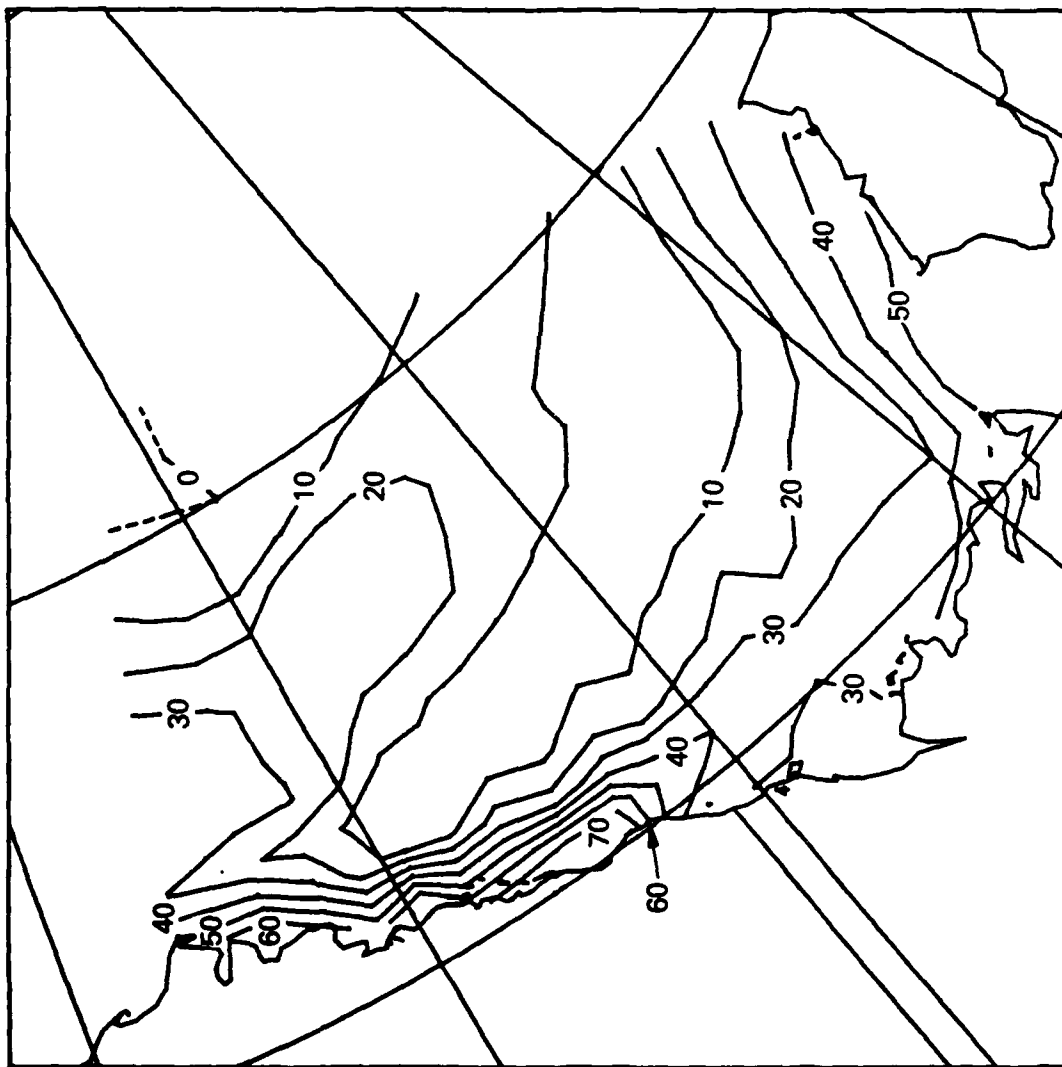


Figure 23. Power Dissipated by Ice p_D on February 7. All Contour Levels in mW/m^2 .

DATE
FILMED
-8